

Oxygen Transport Ceramic Membranes

Quarterly Report

January-April 2001

By:

Dr. Sukumar Bandopadhyay
and
Dr. Nagendra Nagabhushana

School of Mineral Engineering
University of Alaska Fairbanks

Issued: May, 2001

DOE Award # DE-FC26-99FT400054

University of Alaska Fairbanks
School of Mineral Engineering
Brooks 209
Fairbanks, AK 99775

DISCLAIMER

This report was prepared as an account of work sponsored by an agency of the United States Government. Neither the United States Government nor any agency thereof, nor any of their employees, makes any warrantee, express or implied, or assumes any legal liability or responsibility for the accuracy, completeness, or usefulness of any information, apparatus, product, or process disclosed, or represents that its use would not infringe privately owned rights. Reference herein to any specific commercial product, process, or service by trade name, trademark, manufacturer, or otherwise does not necessarily constitute or imply its endorsement, recommendation, or favoring by the United States Government or any agency thereof. The views and opinions of the authors expressed herein do not necessarily state or reflect those of the United States Government or any agency thereof.

Executive Summary

Conversion of natural gas to liquid fuels and chemicals is a major goal for the Nation as it enters the 21st Century. Technically robust and economically viable processes are needed to capture the value of the vast reserves of natural gas on Alaska's North Slope, and wean the Nation from dependence on foreign petroleum sources. Technologies that are emerging to fulfill this need are all based syngas as an intermediate. Syngas (a mixture of hydrogen and carbon monoxide) is a fundamental building block from which chemicals and fuels can be derived. Lower cost syngas translates directly into more cost-competitive fuels and chemicals.

The currently practiced commercial technology for making syngas is either steam methane reforming (SMR) or a two-step process involving cryogenic oxygen separation followed by natural gas partial oxidation (POX). These high-energy, capital-intensive processes do not always produce syngas at a cost that makes its derivatives competitive with current petroleum-based fuels and chemicals.

In the mid 80's BP invented a radically new technology concept that will have a major economic and energy efficiency impact on the conversion of natural gas to liquid fuels, hydrogen, and chemicals.¹ This technology, called Electropox, integrates oxygen separation with the oxidation and steam reforming of natural gas into a single process to produce syngas with an economic advantage of 30 to 50 percent over conventional technologies.²

The Electropox process uses novel and proprietary solid metal oxide ceramic oxygen transport membranes [OTMs], which selectively conduct both oxide ions and electrons through their lattice structure at elevated temperatures.³ Under the influence of an oxygen partial pressure gradient,

¹Mazanec, T. J.; Cable, T. L.; Frye, J. G., Jr.; US 4,793,904, 27 Dec **1988**, assigned to The Standard Oil Company (now BP America), Mazanec, T. J.; Cable, T. L.; US 4,802,958, 7 Feb **1989**, assigned to the Standard Oil Co. (now BP America), Cable, T. L.; Mazanec, T. J.; Frye, J. G., Jr.; European Patent Application 0399833, 24 May **1990**, published 28 November **1990**.

²Bredesen, R.; Sogge, J.; "A Technical and Economic Assessment of Membrane Reactors for Hydrogen and Syngas Production" presented at Seminar on the Ecol. Applic. of Innovative Membrane Technology in the Chemical Industry", Cetraro, Calabria, Italy, 1-4 May **1996**.

³Mazanec, T.J., *Interface*, **1996**; Mazanec, T.J., *Solid State Ionics*, 70/71, **1994** 11-19; "Electropox: BP's Novel Oxidation Technology", T.J. Mazanec, pp 212-225, in "The Role of Oxygen in Improving Chemical Processes", M. Fetizon and W.J. Thomas, eds, Royal Society of Chemistry, London, **1993**; "Electropox: BP's Novel Oxidation Technology", T.J. Mazanec, pp 85-96, in "The Activation of Dioxygen and Homogeneous Catalytic Oxidation", D.H.R. Barton, A. E. Martell, D.T. Sawyer, eds, Plenum Press, New York, **1993**; "Electrocatalytic Cells for Chemical Reaction", T.J. Mazanec, T.L. Cable, J.G. Frye, Jr.; *Prep Petrol Div ACS*, San Fran, **1992** 37, 135-146; T.J. Mazanec, T.L. Cable, J.G. Frye, Jr.; *Solid State Ionics*, **1992**, 53-56, 111-118.

oxygen ions move through the dense, nonporous membrane lattice at high rates with 100 percent selectivity. Transported oxygen reacts with natural gas on the fuel side of the ceramic membrane in the presence of a catalyst to produce syngas.

In 1997 BP entered into an OTM Alliance with Praxair, Amoco, Statoil and Sasol to advance the Electropox technology in an industrially sponsored development program. These five companies have been joined by Phillips Petroleum and now are carrying out a multi-year \$40+ million program to develop and commercialize the technology. The program targets materials, manufacturing and engineering development issues and culminates in the operation of semi-works and demonstration scale prototype units.

The Electropox process represents a truly revolutionary technology for conversion of natural gas to synthesis gas not only because it combines the three separate unit operations of oxygen separation, methane oxidation and methane steam reforming into a single step, but also because it employs a chemically active ceramic material in a fundamentally new way. On numerous fronts the commercialization of Electropox demands solutions to problems that have never before been accomplished. Basic problems in materials and catalysts, membrane fabrication, model development, and reactor engineering all need solutions to achieve commercial success.

Six important issues have been selected as needing understanding on a fundamental level at which the applied Alliance program cannot achieve the breadth and depth of understanding needed for rapid advancement. These issues include

1. Oxygen diffusion kinetics (University of Houston)
2. Grain structure and atomic segregation (University of Illinois - Chicago)
3. Phase stability and stress development (University of Missouri - Rolla)
4. Mechanical property evaluation in thermal and chemical stress fields (University of Alaska Fairbanks)
5. Graded ceramic/metal seals (Massachusetts Institute of Technology)

Statement of Work

Task 1 Design, fabricate and evaluate ceramic to metal seals based on graded ceramic powder / metal braze joints.

- Task 2 Evaluate the effect of defect configuration on ceramic membrane conductivity and long term chemical and structural stability.
- Task 3 Determine materials mechanical properties under conditions of high temperatures and reactive atmospheres.
- Task 4 Evaluate phase stability and thermal expansion of candidate perovskite membranes and develop techniques to support these materials on porous metal structures.
- Task 5 Assess the microstructure of membrane materials to evaluate the effects of vacancy-impurity association, defect clusters, and vacancy-dopant association on the membrane performance and stability.
- Task 6 Measure kinetics of oxygen uptake and transport in ceramic membrane materials under commercially relevant conditions using isotope labeling techniques.

This is the third quarterly report on oxygen Transport Ceramic Membranes. In the following, the report describes the progress made by our university partners in Tasks 1 through 6, experimental apparatus that was designed and built for various tasks of this project, thermodynamic calculations, where applicable and work planned for the future

Task 1 & 2 Development of Ceramic Membrane/Metal Joints

Prof. Thomas W. Eagar, Dr Harold R Larson,
Mr Raymundo Arroyave and Ms Jocelyn L. Wiese

ABSTRACT

The mechanical properties of model systems were analyzed. A reasonably accurate finite element model was implemented and a rational metric to predict the strength of ceramic/metal concentric joints was developed. The mode of failure of the ceramic/metal joints was determined and the importance of the mechanical properties of the braze material was assessed. Thermal cycling experiments were performed on the model systems and the results were discussed. Additionally, experiments using the concept of placing diffusion barriers on the ceramic surface to limit the extent of the reaction with the braze were performed. It was also observed that the nature and morphology of the reaction zone depends greatly on the nature of the perovskite structure being used. From the experiments, it is observed that the presence of Cr in the Fe-occupied sites decreases the tendency of Fe to segregate and to precipitate out of the lattice. In these new experiments, Ni was observed to play a major role in the decomposition of the ceramic substrate.

Mechanical Properties of the Joints

Testing techniques are being developed to measure and understand the mechanical properties of concentric metal-to-ceramic joints. A model system of alumina tubes brazed around nickel- and iron- based alloys using Ticusil™ (Ag-Cu-Ti) brazing alloy has been used as a model system. The testing and analytical methods that have been developed will be applied to the “perovskite/Haynes 230® system once brazing alloys have been developed for those materials and mechanical property data for the ceramic is available.

The previous report, issued January 2001, presented the following conclusions and observations regarding the understanding of the mechanical behavior of concentric metal-to-ceramic joints:

- The residual stresses resulting from CTE mismatch between the base metal and ceramic clearly degrade the strength of the joints.
- The majority of the shear-tested joints failed in a ductile manner; however a subset of joints failed in a brittle manner in which the ceramic component cracked.
- A peak load was supported when the joint length was 0.25”. Absolute strength decreased with joint length. Joint shear strength also decreased with joint length.
- Both the CTE mismatch between substrates and yield strength of the base metal appear to influence joint strength [in addition to the joint-length affect].
- The use of FE models to predict [theoretical] joint strength is promising.

Additionally, the following tasks were listed as “future work”.

1. The use of the finite element model as a predictive tool will be refined.
2. The anomalous behavior of Invar-alumina joints will be investigated.
3. The effect of thermal cycling on joint strength will be investigated.

This report addresses these three tasks while building upon the previous conclusions.

Use of the Finite Element Model as a Tool to Predict Joint Shear Strength

A finite element model was built using ABAQUS to simulate the residual stresses that develop in the joint during cooling from 780C to room temperature. The residual stresses, as well as elastic⁴ and plastic⁵ strain energy present in each joint component (ceramic, base metal, filler metal) were calculated in the model. Models were developed for the four base metal – alumina combinations, and in the same geometries as the experimental shear-tested samples.

A previous uncertainty was how to properly model the material behavior of the base metal. A number of models discussed in the literature model the base metal as linear elastic. When this behavior is used for the base metal in our model, though, the residual stresses present in the base metal of the joint far exceed the known yield stress of the base metals. Since the residual stresses are large enough to cause plastic deformation, the plastic behavior of the base metal must be accounted for in the model; the simplest way to do this is to model the base metal as perfectly plastic.

The majority of the shear-tested joints failed through the filler metal, as no visible cracking of the ceramic was seen in these joint after the maximum load was supported. This failure mechanism was confirmed upon examination of a subset of failed joints with the SEM. Figure 1 shows the cross-section of two different shear tested joints that exhibited the ductile failure mode. The deformation of the filler metal seen in these micrographs substantiates the claim that the failure of these joints occurs in the filler metal. It is also obvious from these micrographs that the microstructure of the filler metal is different in the two joints, which were made with different

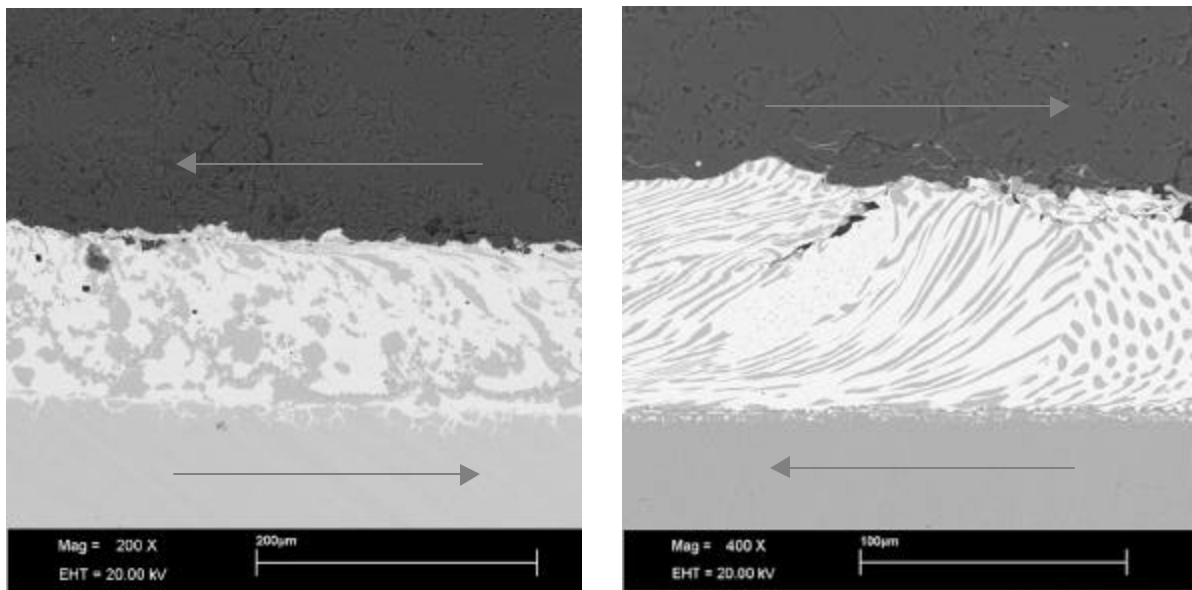


Figure 1: Shearing of filler metal in shear-tested joints. Arrows indicate the direction of applied force. (L) Alumina-304 Stainless Steel. (R) Alumina-Hastellov

⁴ Elastic strain energy, the integral of stress over a displaced area, is a scalar quantity that can be used as a metric to describe the amount of residual stress present in the joint, or any specific component of the joint. This energy can be recovered when the stress is relieved.

⁵ Plastic strain energy is the energy dissipated during plastic deformation. This energy cannot be recovered.

base metals. Unique microstructures were also observed in the joints made between alumina and Inconel 600 or Invar. Much of the variation can be attributed to the amount of nickel present in the filler metal; nickel and copper are completely soluble so nickel from the base metal tended to dissolve into the filler metal, altering the morphology of the filler metal. Iron and copper are immiscible, so a similar effect was not observed joints made with 304 Stainless Steel, a high-iron, low-nickel alloy.

From these observations, it was determined that the base metal should be modeled as perfectly plastic, and the strain energy present in the filler metal should be used as the metric. However, it was not empirically clear which component of the strain energy (elastic, plastic, or total) in the filler metal was to be used as the metric. The relationship between joint length and each component of strain energy in the filler metal was calculated from the data generated by the models, for each type of joint. The theoretical amount of strain energy present in each shear-tested joint was calculated from these relationships.⁶

Since it is the residual stresses in a metal-to-ceramic brazed joint that degrade the strength of the

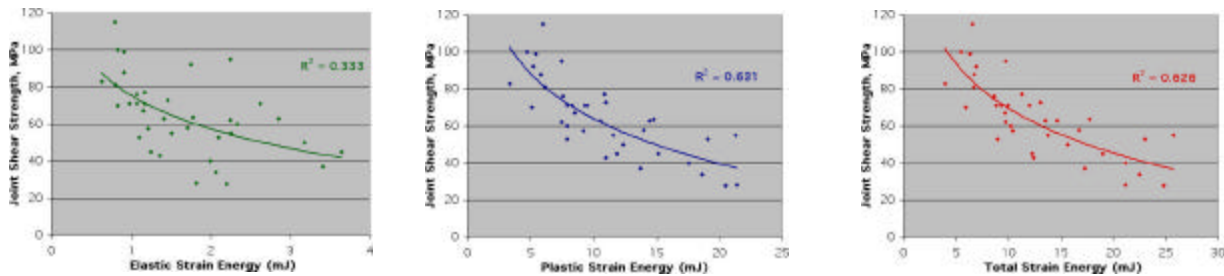


Figure 2: Correlations between measured joint shear strength and calculated elastic, plastic, and total strain energy in the filler metal.

joint, there ought to exist a correlation between strain energy and joint shear strength. Furthermore, since residual stresses are a function of joint geometry and materials, this correlation should hold for joints made with different substrates. The strain energy – joint strength data for all samples were plotted together, and R^2 values calculated (Figure 2). Both the plastic strain energy and total strain energy present in the filler metal correlate quite well with joint strength.

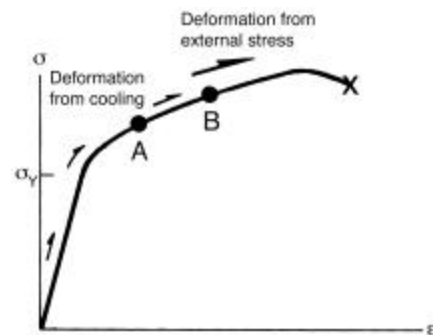


Figure 3: The stress state of the filler metal in two joints, A and B, plotted on the stress-strain curve of a

To understand why plastic deformation of the filler metal (quantified by the plastic strain energy) decreases the strength as measured by the shear test, consider two brazed joints, A and B. The degree of deformation of the filler

⁶ It should be noted that the finite element model did not account for the differences in microstructure observed in the filler metal of the joints made with different base metals; the model assumed that the filler metal in all joints was identical.

metal in these joints is marked on the stress-strain curve for hypothetical filler metal in Figure 3. The filler metal in Joint B has been strained more than in Joint A because, for example, the lap joint length of Joint B was longer or there was a greater CTE mismatch between its substrates. The additional load applied to the filler metal during the shear test causes additional plastic deformation of the filler metal, and movement along the stress-strain curve toward failure. The shear test measures the total additional load needed to stress the filler metal in the joint to failure. Since the filler metal in Joint A was less deformed than that in Joint B before the shear test, it will take more external load to stress the filler metal in Joint A to failure; thus Joint A will have a higher calculated shear strength.

Anomalous Behavior of Invar-Alumina Joints

Many of the short and long joints made with Invar and alumina cracked in the ceramic during the shear test, while joints made with the same materials that were of intermediate length failed in the filler metal. Short joints made between Hastelloy B2 also cracked the ceramic. One possible reason why the short joints (made either with Invar or Hastelloy B2) failed in the ceramic was that the filler metal in these joints did not deform much during cooling. As the joint was stressed in shear, the filler metal sheared plastically, but since it had not deformed much during cooling it could withstand more force before failing; so much force that the ceramic failed before the filler metal.

The theory that suggests why some of the short joints failed in the ceramic does not adequately explain why some of the long joints (length greater than 0.30") made with Invar failed in the ceramic. These joints had about the same shear strength at failure as the intermediate length joints. It is possible that the failure of joints made from Invar is not controlled by the strain energy present in the filler metal, as it may be only the low temperature CTE mismatch that controls the true strain energy present in the joint⁷. Since Invar has unique behavior at low temperatures when compared to most metals, including the other three in the study, so comparisons made between joints made with Invar and the other materials may not be completely valid. In fact, when the data for joints made with Invar is removed from the total data set, the correlation between total strain energy in the filler metal and joint strength improves by 16% to an R^2 of 0.7319; this correlation is as good as the correlations between the strain energy and joint strength for a single type of joint. This correlation is referred to as the revised total strain energy correlation later in this report.

Effect of Thermal Cycling on Joint Strength

The ceramic membrane seals would be subjected to thermal cycles during the life of the reactor system. The effect of thermal cycling on joint strength was studied by subjecting brazed joints to thermal cycles, then measuring their shear strength. The sample geometry and testing method were identical to that used in the joint strength study.

A lap joint length of 0.25" was chosen for the thermal cycling study because joints of that length supported the greatest absolute load in the previous strength tests. Joints made between Hastelloy B2, Inconel 600, and 304 Stainless Steel were tested; joints made with Invar were excluded for simplicity. Joints were exposed to either 2 or 5 cycles between 150C and 650C, ramping and cooling at a rate of 10C/minute. The cooling rate below ~300C was slower than

⁷ Suganuma et al. Journal of Materials Science, 22, 2702, (1987).

10C/minute, though, because it was controlled by the ambient cooling of the furnace. Two hours were allowed between cycles to ensure that the sample had cooled to 150C before being reheated.

The shear strengths of the joints that were subjected to thermal cycles are tabulated in the tables below. The measured strength of each joint is compared to the ideal strength of a non-cycled joint, calculated from the strain energy of the joint, by dividing the measured strength by the “ideal” calculated strength. It should be mentioned that the measured/ideal strength ratio for the non-thermal-cycled joints of overlap length 0.250” (from the previous set of experiments, the data from which was used to derive the relationship between strain energy and joint strength) ranged between 0.69 – 1.25.

The strengths of the joints subjected to two thermal cycles, made with Inconel 600 or Hastelloy B2, clearly degraded. The joints made with 304 Stainless Steel, did not appear to degrade; however, the failure mode changed from ductile failure through the filler metal to brittle failure that cracked the ceramic. Interestingly, joints subjected to five thermal cycles had higher shear strength than joints subjected to two thermal cycles: the joints made with Hastelloy B2 or Inconel 600 were strong as joints that had not been subjected to any thermal cycles and the shear strength of joints made with 304 Stainless Steel actually increased. The failure mode of all joints was brittle failure through the ceramic.

Table 1: Strength of Brazed Joints after 2 Thermal Cycles

Base Metal	Overlap Length (in.)	Ideal Strength* (MPa)	Measured Strength (MPa)	Measured / Ideal	Failure Mode
Hastelloy B2	0.250	76	43	0.56	Ductile
Hastelloy B2	0.257	74	39	0.53	Ductile
Inconel 600	0.254	62	39	0.63	Ductile
Inconel 600	0.253	63	30	0.48	Ductile
304 Stainless	0.247	67	48	0.72	Brittle
304 Stainless	0.245	68	125	1.84	Brittle

* Estimated shear strength after zero thermal cycles predicted by the revised total strain energy correlation

Table 2: Strength of Brazed Joints after 5 Thermal Cycles

Base Metal	Overlap Length (in.)	Ideal Strength* (MPa)	Measured Strength (MPa)	Measured / Ideal	Failure Mode
Hastelloy B2	0.258”	73	57	0.78	Brittle
Hastelloy B2	0.252”	75	78	1.04	Brittle
Inconel 600	0.224”	73	68	0.93	Brittle
Inconel 600	0.249”	64	Testing error	--	--
304 Stainless	0.255”	65	112	1.67	Brittle
304 Stainless	0.250”	67	112	1.72	Brittle

* Estimated shear strength after zero thermal cycles predicted by the revised total strain energy correlation

The observation that subjecting the metal-to-ceramic joints to thermal cycles does not necessarily degrade their shear strength is counter-intuitive, since the repetitive, mismatched, expansions and contractions should increase residual stress and fatigue the joint components. Joints made with different base metals responded to the thermal cycles differently; the microstructure of the filler metal also varied depending on the base metal. It is possible that the microstructure and mechanical properties of the filler metal, rather than the mechanical properties of the substrates, control how the strength of the joint changes after being subjected to thermal cycles.

Conclusions:

The following new conclusions have been reached regarding the mechanical properties of the joints studied:

- The tensile residual stresses that develop in the base metal of the joint can be large enough to induce plastic deformation; hence, the plastic behavior of the base metal must be accounted for when modeling the joint.
- The filler metal plastically deforms to accommodate the property mismatch between the base metal and ceramic, and is in a state of triaxial tension after cooling. Both the plastic and total strain energy, quantitative indicators of the degree of elastic and plastic deformation of the filler metal as calculated by a finite element model, are predictive indicators of the shear strength of the filler metal in the joint. Since the joints fail in the filler metal, these strain energy values can be used to predict joint shear strength.
- The coefficient of thermal expansion between the base metal and ceramic is the most important physical property influencing the strain energy in the filler metal and the theoretical strength of the joints. The yield stress of the base metal is of secondary importance.
- The morphology of the filler metal in joints varied with the base metal. Nickel from the base metal tended to dissolve into the filler metal, altering the microstructure.
- Thermal cycling did not monotonically degrade the strength of the joints, however the failure mode of the joints changed from ductile to brittle after five thermal cycles. Preliminary results suggest that the microstructure and mechanical properties of the filler metal play a dominant role in determining joint strength after being subjected to thermal cycles, but further research should be done in this area.

Perovskite/Metal Interactions

Over the past months, we have continued experimentation regarding the interactions between Ni-B based alloys and perovskite substrates. Because of the range of operating temperatures required for the seal, as well as due to the oxidation resistance required by the interlayer material used for the joining process, Ni-based alloys have been identified as the optimal metallic system that could potentially work. However, despite considerable experimentation with these alloys, it has been observed that the reactions at the ceramic/metal interface tend to affect the stability of the ceramic substrate largely.

In previous experiments with $\text{La}_{0.6}\text{Sr}_{0.4}\text{FeO}_3$, it has been observed that the reaction zone at the ceramic substrate was approximately 100 microns thick. The ceramics used previously had been

pressureless sintered at high temperatures. In these past experiments, it was observed that the main result from the reaction between Ni-based brazing alloys and the ceramic substrate was the segregation of Fe from the ceramic lattice:

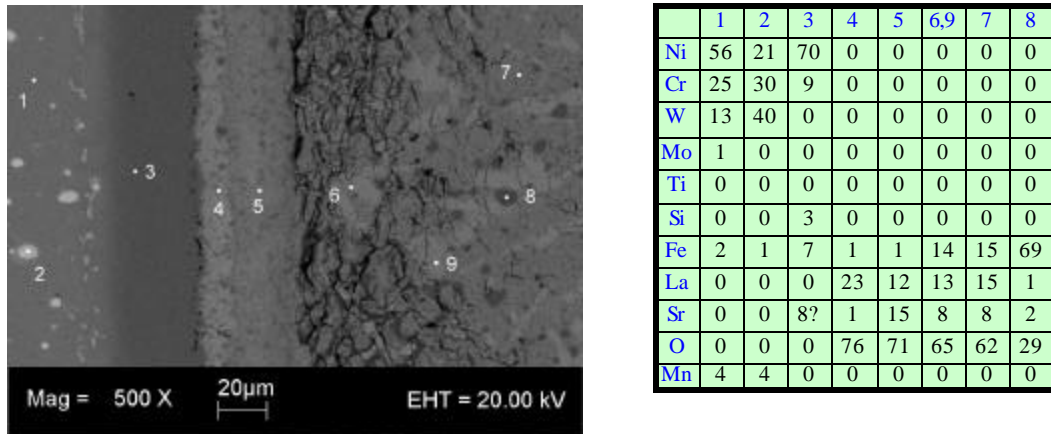


Figure 4 Perovskite/Metal Interactions $\text{La}_{0.6}\text{Sr}_{0.4}\text{FeO}_3$

In these experiments, Fe “islands” precipitated in the region close to the reaction zone and extensive migration of Sr and La towards the interface with the metal was observed. Despite promising results, it was observed that there was a tendency for crack formation at the region close to the interface with the braze. This crack formation was attributed to the extensive decomposition undergone by the ceramic substrate when in contact with the braze.

As it became evident that the extent of the reaction needed to be limited somehow, the focus of the experimental program was switched to the creation of diffusion barriers on top of the ceramic substrate. These diffusion barriers would be able to still promote adhesion to the perovskite surface but at the same time would limit the extent of the reaction with the braze.

A series of experiments was devised to determine the potential use of diffusion barriers to limit the extent of the reaction at the ceramic/metal interface. Because of external factors, the ceramic used in this occasion was different from the first series of experiments, so no direct comparison between previous and new results was possible. For the diffusion-barrier experiments, the ceramic used was $\text{La}_{0.2}\text{Sr}_{0.8}\text{Cr}_{0.2}\text{Fe}_{0.8}\text{O}_3$. A nickel-based super alloy was used as the metal substrate and the same Ni-B brazing alloy was used as the bonding interlayer.

The samples were cut in 0.5” Dia x 0.1” thick disks, and then polished to 600 GRIT. After that, the samples were ultrasonically cleaned in isopropyl alcohol. The ceramic disks were conditioned in a N_2 atmosphere at 500 C for 2 hours before the experiments. For the actual joining experiments, the same high-temperature vacuum furnace was used. Temperature ramping up and down was controlled to minimize the possibilities of joint failure due to thermal shock. To keep the joint in place while joining, a slight pressure was applied.

To test the concept of diffusion barriers, a Cr layer was deposited on top of the ceramic substrate using a magnetron-sputtering unit. A layer of around 10 microns was deposited on the perovskite disks. For the experiments, three different cases were studied:

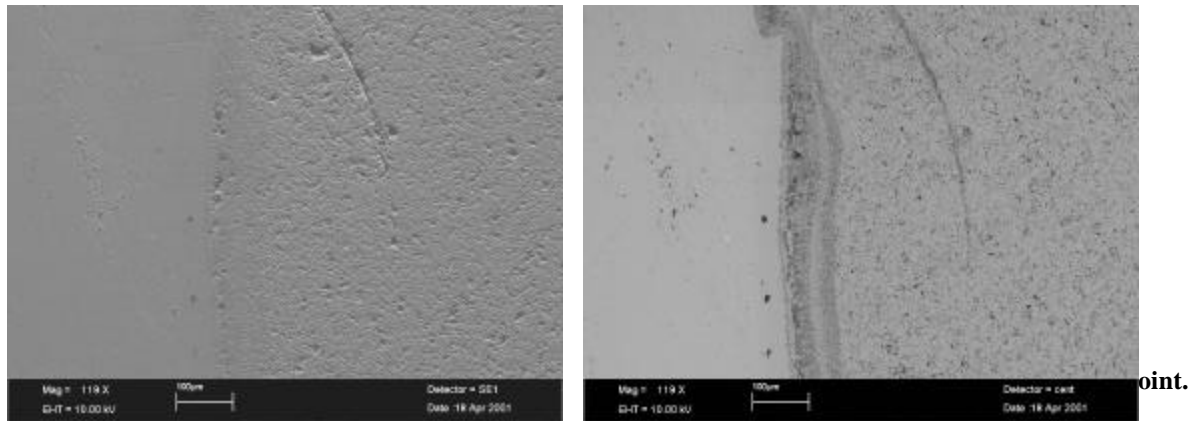
The first one consisted in doing a two-step brazing operation in which the joint at first would be brought to a temperature (950 C) lower than the solidus of the Ni-B interlayer. Leaving the joint at that temperature for about 15 minutes would allow enough time for the reaction between the perovskite disk and the Cr layer so a stable Cr_2O_3 layer could be formed. After this, the temperature would be raised to 1100 C, a temperature high enough to allow the melting of the Ni-B interlayer. After 15 minutes at this temperature, the sample was cooled to room temperature at a rate low enough to avoid thermal shock (10 degrees per minute).

Another option explored was to form the chromium oxide layer before the joining experiment took place. For this, perovskite disks with Cr layers were put in a slightly oxidized atmosphere at 550 C for 2 hours. An oxide layer was observed to form on top of the perovskite disks. The purpose of this experimental approach was to take advantage of the fact that Cr_2O_3 is usually insoluble in other oxides as well as in liquid metals. Once the oxide layer was formed, the joint would be raised to 1100 C in the vacuum furnace for 15 minutes, as in the experiments described above.

Finally, to establish a base case for comparison, a perovskite disk without any sputtered Cr-layer was joined to a Ni-based base metal using the same Ni-B interlayer. The same heating and cooling rates were used.

Below we present the preliminary results concerning the experiments described above:

Perovskite / Cr / Ni-B / Inconel:



From the figures above, it can be observed that an interface was formed between the braze metal and the perovskite surface. Contrary to our expectations, though, the Cr layer sputtered on the ceramic surface was somehow dissolved by the braze and the reaction with the ceramic was rather extensive (the reaction zone was almost as wide as in the previous series of experiments). It was also observed that the nature of the interactions between the ceramic and the braze were different from those observed with the $\text{La}_{0.6}\text{Sr}_{0.4}\text{FeO}_3$ perovskite:

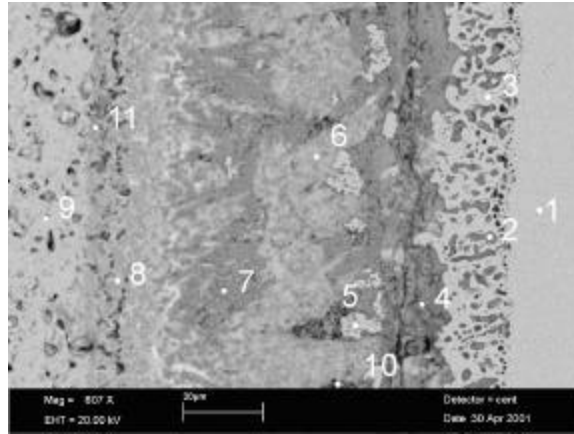


**Figure 7 Perovskite/Cr/Ni-N/Inconel Joint.
SEM , backscattered image. 807x**

By comparing Figures 4 and 7, it is evident that the morphology and nature of the reaction products at the ceramic/braze interface differ greatly. For example, no Fe localized segregation and “island” formation was observed in this new series of experiments. To explain the results of the previous experiments, it was hypothesized that the low Fe content of the braze alloy created at large driving force for the segregation of Fe towards the interface. In these new experiments, however, no such extensive segregation towards the interface was observed.

Another important difference between the reactions observed in the previous experiments and that observed in these $\text{La}_{0.2}\text{Sr}_{0.8}\text{Cr}_{0.2}\text{Fe}_{0.8}\text{O}_3$ /Metal joints is the absence of a La-O layer in direct contact with the braze. When La is the major component in the A sites of the perovskite structure, the formation of La-O compounds appears very likely. When this is not the case, however, La appears to segregate towards the perovskite (see figure and table above). Another important difference is the formation of a complex Ni-Cr-O (point 3) layer in direct contact with the braze. This implies that local reduction of the perovskite surface is taking place. The local oxygen chemical potential at the interface must thus be such that decomposition of the perovskite structure is favorable ($p\text{O}_2$ around 10^{-16}). A very interesting feature of this layer is the presence of highly metallic precipitates with Ni (point 2) as their major component (96%). As we go deeper into the reaction zone, Sr appears as a major component of the reaction products. La, on the other hand, does not appear at all in this region (point 4). It has been observed that this region is most likely to be the nucleation site of cracks that run parallel to the ceramic/metal interface and further characterization of the reaction products in this area appears to be necessary.

At approximately 30 microns from the ceramic/metal interface, no noticeable changes in composition can be observed. In fact, it is not unreasonable to infer that the only difference between this region and the bulk perovskite ceramic is the presence of brazing alloy inside the pores of the material:

	1	2	3	4	5	6	7	8	9	10	11
Ni	81.6	96.5	25.5	4.7	4.0	17.3	4.0	1.1		4.1	1.5
Cr	8.2	1.3	11.6	9.8	3.4	2.9	2.4	0.8	3.1	3.0	3.2
Fe	4.6	2.1	6.0	12.4	9.2	8.2	9.5	4.8	12.6	9.0	12.3
Sr				13.8	9.4	6.5	10.7	15.6	16.3	9.7	11.4
La					0.1	2.6	1.4	5.7	4.2	3.5	3.0
O			56.9	59.4	73.9	62.4	72.0	72.1	63.8	70.7	68.6
Si	5.4										

When comparing the results of both

series of experiments, it appears evident that Ni appears to be playing a major role in the these $\text{La}_{0.2}\text{Sr}_{0.8}\text{Cr}_{0.2}\text{Fe}_{0.8}\text{O}_3$ /Metal experiments, which is not the case in the La-Sr-Fe-O/Metal reactions. Ni has been observed to be present at a depth of 60 microns into the reaction zone. This could be explained by the fact that the La-Sr-Cr-Fe-O perovskite samples presented an extremely high porosity. The braze, therefore, would be able to infiltrate the ceramic to a large extent. The porosity is thus “healed” by the presence of this liquid metal. The problem with this, though, is that the difference in expansion coefficients between the porous matrix and the filling medium can lead to a weakening of the matrix, as cooling and heating cycles proceed.

Perovskite / Cr_2O_3 / Ni-B / Inconel:

Contrary to what we had expected, the experiments in which a pre-oxidized layer of sputtered Cr was deposited on the ceramic substrate yielded somewhat similar results, as can be seen in the figure below:

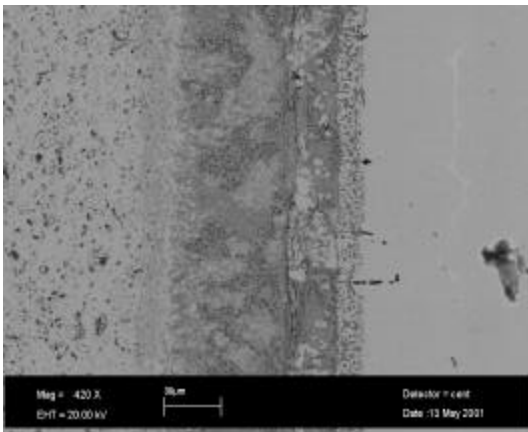


Figure 8. Perovskite/ Cr_2O_3 /Braze Reactions

From the figure above, it can be seen that the reaction sequence and morphology is identical to the two-steps brazing experiment, in which no pre-oxidation of the Cr layer was done. Additionally, it was also observed that crack nucleation took place in almost the same region. In both cases, the sputtered layer seems to have been dissolved by the braze, and therefore, its effectiveness is doubtful.

The concept of placing a diffusion barrier to decrease the extent of the reaction between the brazing alloy and the perovskite structure needs to be further explored and different materials must be evaluated. Experiments with other materials and joining procedures are under way.

Conclusions

From the experiments described above, the following can be concluded:

- The nature and morphological features of the reaction zone differ greatly with the nature of the Perovskite material. In these new experiments no Fe segregation was observed and La-O compounds did not form at the ceramic/braze interface.
- In contrast to the previous experimental evidence, Ni appears to be playing a major role in the decomposition of the ceramic material. The fact that a Ni-Cr-O phase was formed at the interface with the braze, suggests that locally, the oxygen partial pressure was such that decomposition of the ceramic took place.
- The high porosity of the ceramic samples used resulted in high infiltration by the nickel-based brazing alloy. In fact, nickel was observed at depths of 60 microns from the ceramic/braze interface. This infiltration may result in further mechanical damage of the ceramic due to the differences in coefficients of thermal expansion between the nickel alloy and the perovskite matrix. To increase the chances of getting reliable ceramic/metal seals, the porosity of the ceramic substrate must be reduced or an effective diffusion barrier must be implemented.
- It was observed that the intended diffusion barriers deposited on the ceramic surface were not effective. The brazing alloy appeared to be able to dissolve the layers.
- Further experimentation with diffusion barriers using other materials -probably highly refractory metals or compatible and more stable ceramic oxides- must be done.

TASK 3: Determine material mechanical properties under conditions of high temperature and reactive atmosphere

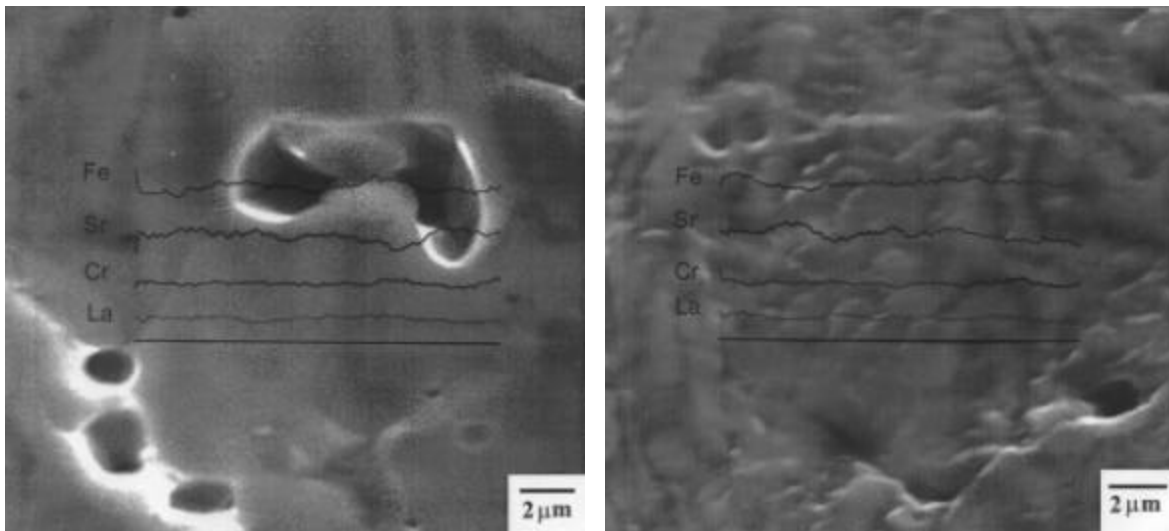
Prof. Sukumar Bandopadhyay & Dr. Nagendra Nagabhushana
University of Alaska Fairbanks

Summary

In the previous quarter, strength of La-Sr-Fe-O ceramic tubes in a slightly reducing conditions were reported. Tubes of Cr_2O_3 doped LaSrFeO_3 (20573 (a-f) were tested at 1000°C in Nitrogen environment and results indicate that tubes showed a decrease in strength but with a slight increase in Weibull modulus from as tested samples at room temperature. In this quarter, fracture was extensively characterized and attempts were made to correlate fracture with the microscopic details obtained by Prof. Browning group at UIC. Also initial et of experiments were started to measure strength in a more reducing atmosphere viz. $90\%\text{CO}_2/10\%\text{CO}$.

Fracture Analysis in membranes tubes tested in Nitrogen

Fracture tests were done in nitrogen atmosphere at 1000°C and 25 PSI



Samples tested in reducing conditions also indicated extensive relief between the grains and the grain boundaries. Line scans analysis across the fractured grains (Fig. 1), indicates that the bulk of the grains exhibits the same structural composition as at the room temperature. However, it is observed that grain boundaries are strontium rich while the grains are strontium deficient. This corresponded well with previous observations concluding a build up of strontium at the grain boundaries and the strontium deficient grains acting as acceptors.

(a)

(b)

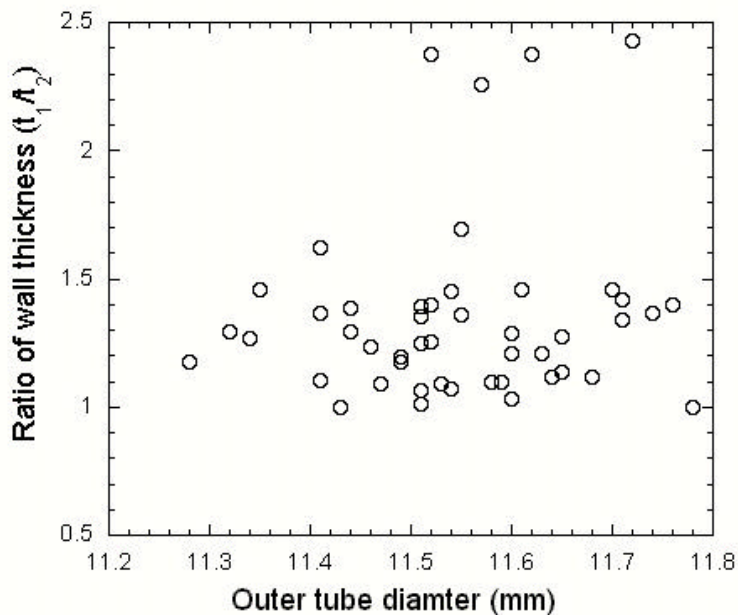
Fig. 1. Line scan across fractured surface indicating the distribution of elements. a) tested at ambient conditions and b) reducing conditions.

Strength of LSFCE tubes in CO₂/CO environment

a) Sample selection and Experimental Procedure

The samples were selected randomly and any dimensional changes in the sample geometry were methodically recorded as outlined in the previous report. The variations in sample dimension used in the present study are as shown in fig.2.

The sample were placed in the autoclave and purged with nitrogen. Purging with nitrogen was done three times and a positive pressure of 25PSI was maintained. The autoclave temperature was raised to 950°C and nitrogen was replaced by CO₂/CO gas mixture. The temperature was then raised to 1000°C and pressure of 25 PSI. The sample was soaked for a period of 15 minutes prior to application of load. Tests were done at 0.5 mm/min as discussed in the previous report.



b) Results

In this period, only the initial results of the strength tests are reported. The average strength of the membrane tubes dropped in comparison to those tested in nitrogen under similar conditions. The membrane tubes indicated fracture strength of 116-130 MPa as compared to 180 MPa in nitrogen. A marked change in the fracture morphology was also observed. The surface were more rough and showed reduced brittleness. Microscopic observation also complemented the macroscopic observation. As shown in fig.3, the grains and precipitates showed marked coarsening as compared to those tested in nitrogen environment. A detailed study will form a part of the next quarterly report.

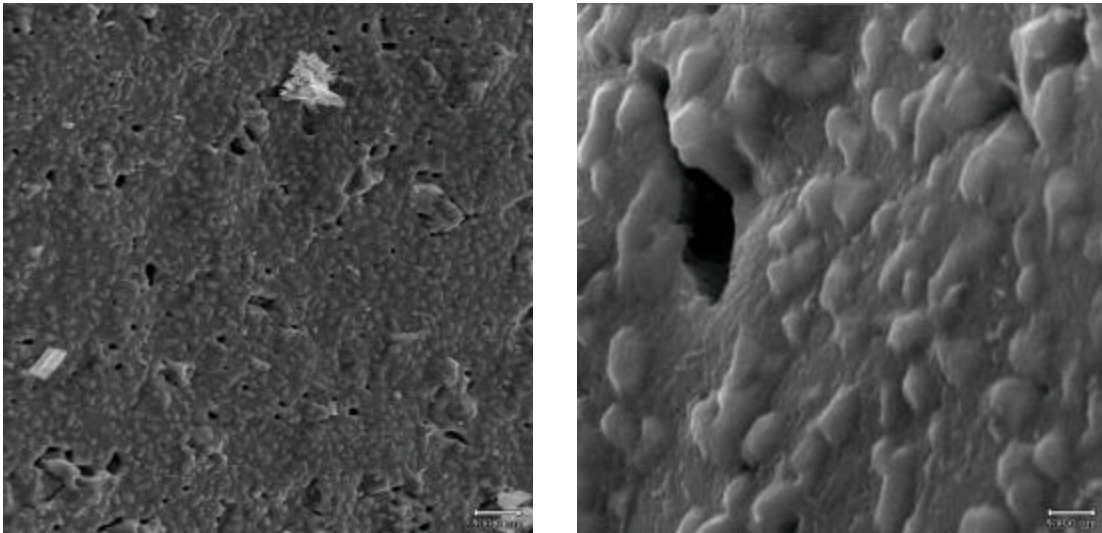


Fig.3 Fracture morphology in samples tested in 90%CO₂/10%CO at 1000°C and 25PSI

Task 4: Preparation and characterization of Dense Ceramic Oxygen Permeable Membrane

Dr. Harlan U. Anderson, Director of EMARC

Dr. Wayne Huebner, Dr. Yixiang Xie

University of Missouri- Rolla

Summary

Two compositions of mixed-cation oxide powder, $\text{La}_{0.60}\text{Sr}_{0.40}\text{Fe}_{0.85}\text{Ga}_{0.15}\text{O}_3$ (A) and $\text{La}_{0.20}\text{Sr}_{0.80}\text{GaO}_3$ (B) were prepared by a modified Pechini liquid mixing method [1, 2]. While X-ray diffraction patterns taking on (A) composition show a major Perovskite phase, composition (B) exists as an mixture of La, Sr, and Ga oxides. Neutron diffraction measurement indicates that $(\text{La}_{0.59}\text{Sr}_{0.40})_{0.99}\text{Fe}_{1.0}\text{O}_3$ has a rhombohedral structure at 1000 °C under air condition and under a reducing atmosphere. Peak broadening is evidence of starting phase separation under a strong reducing atmosphere (1000 °C, 90% CO/10% CO₂, log PO₂ = -16.1), a confirmation that previous TGA and thermal expansion measurement also suggest the phase stability with logPO₂ higher than -16.1. The conductivity of $(\text{La}_{0.59}\text{Sr}_{0.40})_{0.99}\text{Fe}_{1.0}\text{O}_3$ shows a p-n transition with decreasing PO₂. Archimedes density measurement [3 – 6] gives its sintered densities to be 3.61-5.95 g/cm³ depending on sintering temperature 800 – 1200 °C, which are 60.0 – 99.3% its theoretical density of 5.99 g/cm³.

Experimental

$\text{La}_{0.60}\text{Sr}_{0.40}\text{Fe}_{0.85}\text{Ga}_{0.15}\text{O}_3$ (A) and $\text{La}_{0.20}\text{Sr}_{0.80}\text{GaO}_3$ (B) were prepared through the same process described in report 1 but at a 800 °C calcination temperature. Disk (sintered at 1200 °C, isostatic press at 45,000 psi) x-ray diffraction measurements were carried out on a SINTAG 2000 x-ray diffractometer. Neutron Diffraction Measurements were done at the Reactor of University of Missouri-Columbia. Disk samples for Neutron Diffraction measurements (wavelength: 1.4875 Å) were reheated at 1000 °C under air, 10% CO/90% CO₂, 50% CO/50% CO₂, and 90% CO/10% CO₂, respectively for 24 hours and quenched under the respect atmospheres. Liquid displacement technique [3-6] was used to measure the densities of the sintered discs. A Sartorius scale was employed. The standard density kerosene used is 0.787 g/cm³. Thermal expansion experiments were done by a modified Orton 1600 dilatometer. The weight losses in different atmosphere were measured using a CAHN TG171. Absolute oxygen content was determined by redox titration of a quenched powder sample from 1000 °C to room temperature in air. Electrical conductivity of a bar was measured using a SI 1286 Electrical Interface (Solartron).

Sintering Process of $(\text{La}_{0.59}\text{Sr}_{0.40})_{0.99}\text{FeO}_3$

Step	Ramp, minute	Temperature, °C	Dwell, minute
1	300	100	300
2	300	200	300
3	300	300	300
4	300	400	300
6	800	800	300
7	50	1200	600

8	60	800	-
9	600	room	-

Quenching process of $(\text{La}_{0.59}\text{Sr}_{0.40})_{0.99}\text{Fe}_{1.0}\text{O}_3$ discs for neutron Diffraction

Atmosphere	Ramp, minute	Temperature, °C	Dwell, hour	Quench to, °C
Air	200	1000	24	25
10% CO/90% CO ₂	200	1000	24	25
50% CO/50% CO ₂	200	1000	24	25
90% CO/10% CO ₂	200	1000	24	25

Results and Discussion

Figure 1, and 2 show the XRD patterns of disk $\text{La}_{0.60}\text{Sr}_{0.40}\text{Fe}_{0.85}\text{Ga}_{0.15}\text{O}_3$ (A) and $\text{La}_{0.20}\text{Sr}_{0.80}\text{GaO}_3$ (B), which indicate major Perovskite phase for (A) and multi-phase of La, Sr, and Ga oxides for (B). Like Zr, and Ce, ionic radius of Ga is rather bigger than that of Fe. Previous research indicated that Zr and Ce doping created phase instability of a Perovskite structure. Composition (B) was made twice and XRD proved it a multi-phase composition. Total substitution of Ga for Fe is not recommended.

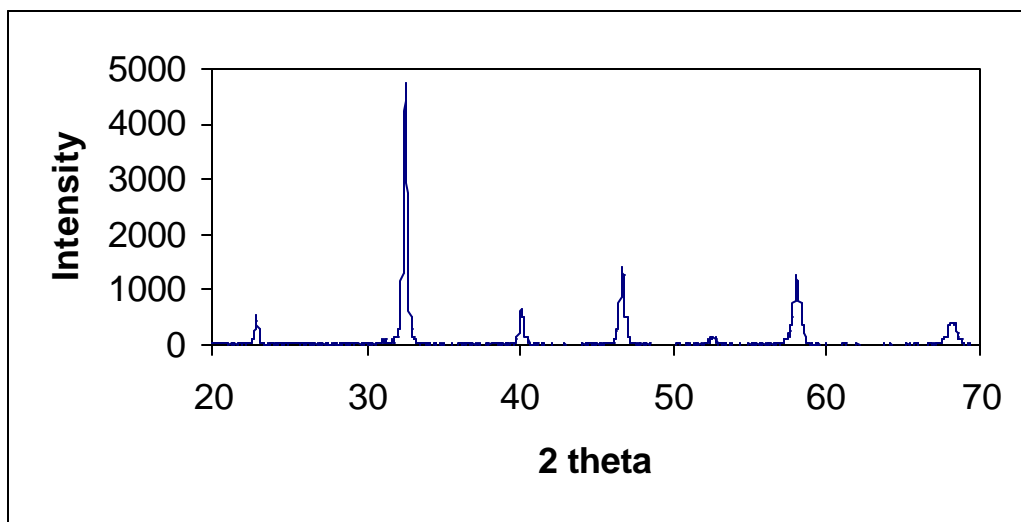


Figure 1. XRD pattern of disk $\text{La}_{0.60}\text{Sr}_{0.40}\text{Fe}_{0.85}\text{Ga}_{0.15}\text{O}_3$ (A), a major Perovskite phase

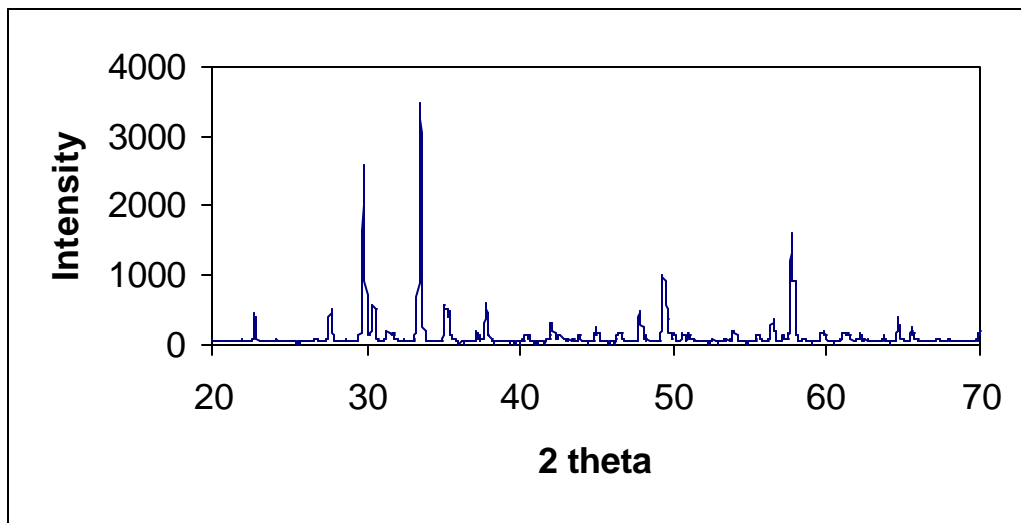


Figure 2. XRD pattern of disk $\text{La}_{0.20}\text{Sr}_{0.80}\text{GaO}_3$ (B), a multi-phase of oxides

Repeated TGA measurement and titration of $(\text{La}_{0.59}\text{Sr}_{0.40})_{0.99}\text{FeO}_{3-\delta}$ determines the oxygen content under different atmospheres at 1000 °C in this material, which is shown in Table 1. The oxygen content difference in this material under Air and 10% CO/90% CO_2 is 0.16 that is big enough to generate the phase transition indicated by ND patterns. Its difference, 0.02, under 10% CO/90% CO_2 and 50% CO/50% CO_2 is small, and respectively there is no significant peak intensity change observed in those two ND patterns. When oxygen loss from stoichiometry reaches 12% under 90% CO/10% CO_2 at 1000 °C ($\log \text{PO}_2$), the composition starts decomposition as XRD and ND data suggested.

Table 1. Equilibrium oxygen content in $(\text{La}_{0.59}\text{Sr}_{0.40})_{0.99}\text{FeO}_{3-\delta}$ at 1000 °C

Atmosphere	3- δ
Air	2.88
N_2	2.82
1% CO/99% CO_2	2.74
10% CO/90% CO_2	2.72
50% CO/50% CO_2	2.70
90% CO/10% CO_2	2.64
99% CO/1% CO_2	2.13* not equilibrium

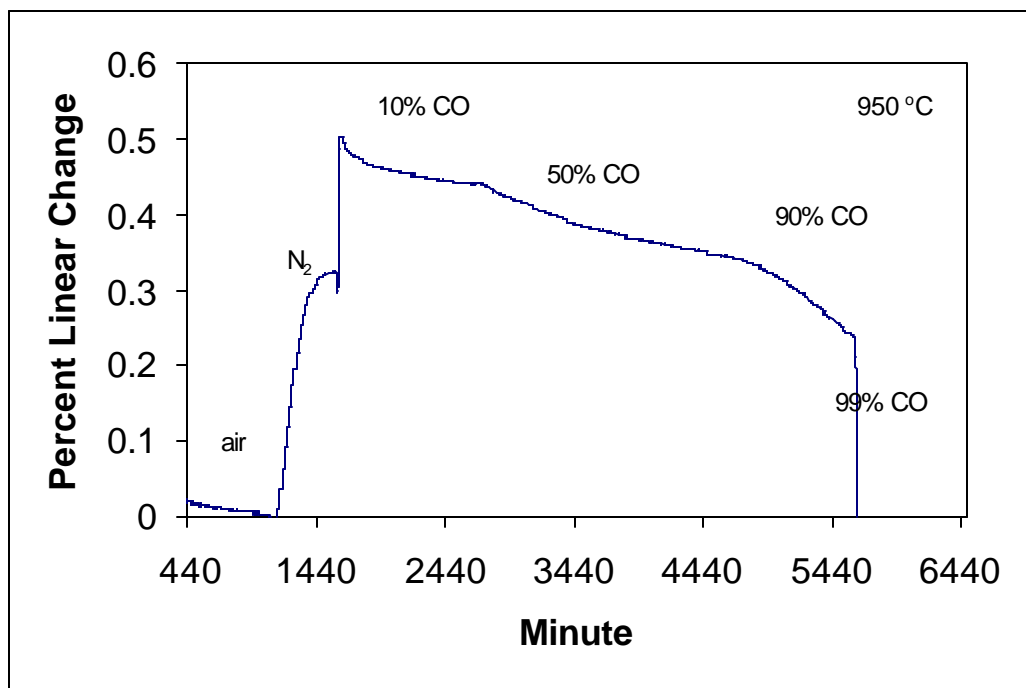


Figure 3. Thermal Expansion of dense $(\text{La}_{0.59}\text{Sr}_{0.40})_{0.99}\text{FeO}_3$

Figure 3 shows thermal expansion of dense $(\text{La}_{0.59}\text{Sr}_{0.40})_{0.99}\text{FeO}_3$, at 950 °C. Equilibrium data of thermal expansion relative to the sample under air condition is listed in Table 2.

Table 2. Thermal Expansion at 950 °C of $(\text{La}_{0.59}\text{Sr}_{0.40})_{0.99}\text{FeO}_3$

Atmosphere (log PO_2)	Linear Change %
Air (-0.68)	0
N_2 (-5)	0.32
10% CO (-13.2)	0.44
50% CO (-15)	0.36
90% CO (-17)	0.24

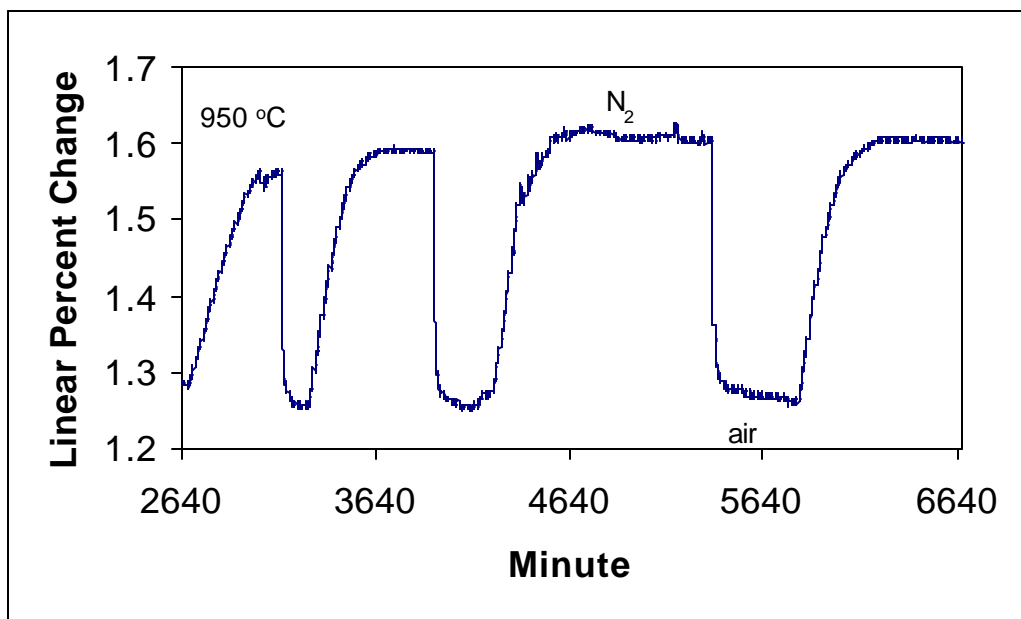


Figure 4. Thermal Expansion of dense $(\text{La}_{0.59}\text{Sr}_{0.40})_{0.99}\text{FeO}_3$

Figure 3 shows reversible thermal expansion of dense $(\text{La}_{0.59}\text{Sr}_{0.40})_{0.99}\text{FeO}_3$, at 950 °C under air- N_2 circulation.

Remeasurement of electrical conductivity of $(\text{La}_{0.59}\text{Sr}_{0.40})_{0.99}\text{FeO}_3$ led to agreement with previous results.

Archimedes density measurement [3 – 6] gives its sintered densities (Table 3) of $(\text{La}_{0.59}\text{Sr}_{0.40})_{0.99}\text{FeO}_3$ to be 3.61-5.95 g/cm^3 depending on sintering temperature 800 – 1200 °C, which are 60.0 – 99.3% its theoretical density of 5.99 g/cm^3 . To reach a dense material for this composition, a sintering temperature will have to be at least 1200 °C.

Table 3.

Sintering temperature, °C	Bulk density, g/cm^3
800	3.61
900	4.01
1000	5.14
1100	5.83
1200	5.94

Composite Structures

In order to put dense films on porous support substrates it is necessary to reduce the diameters at the surfaces and to make the surfaces smoother. Studies have been initiated to achieve these goals.

The initial studies were done using colloidal ceria as the surface treatment layer.

Nanocrystalline cerium oxide powder with an initial grain size of approximately 5nm was produced using an aqueous precipitation processing route. 99.999% cerium (III) nitrate (Alfa Aesar, Inc.) was dissolved in distilled water and precipitated to cerium hydroxide particles using hydrogen peroxide and ammonium hydroxide.

Aqueous colloidal suspensions were prepared by mixing 10 weight percent of CeO₂ powder in pH 4 distilled water (balanced with HNO₃) along with 5 weight percent butoxyethanol to aid in drying and decrease the wetting angle. The butoxyethanol also partially polymerizes due to the acidic content of the solution, and as a consequence aids in increasing the solution viscosity and in the formation of a continuous film. The power was then dispersed in the solution using a high intensity ultrasonic probe for about one hour. The solution was then filtered through a 0.45μm glass fiber filter (Whatman, Inc.) in order to remove any foreign matter.

Thin films of CeO₂ were prepared by spin coating the colloidal suspension on a variety of substrates. Optical quality, both sides polished (0001) oriented sapphires substrates were used for both the optical measurements as well as the DC conductivity measurements.

Films were spun on the prepared substrates at 1500rpm for 30 seconds and subsequently dried at 70°C for about an hour. The films were then heat treated at 350°C for about an hour and cooled back to room temperature after which subsequent coatings could be deposited. Sintering of the porous films was done in a standard furnace using a ramp rate of 5°C/min to the maximum temperature, at which they were held for 2 hours.

The sintered films were characterized according to their grain size, thickness and density using X-ray diffraction, mechanical profilometry, ellipsometry, and UV-Vis spectroscopy, as shown in previous studies. The results as to the grain size, film density and thickness are shown in figures 5-10. Initially, the films have a density of approximately 50% and a grain size of 5nm after 400°C and densify to 85% with a grain size of 60nm after annealing at 1000°C. The X-ray diffraction patterns of CeO₂ samples on sapphire substrates annealed at different temperatures showed that the films are single-phase fluorite structured and show no reaction with the substrate over the investigated temperatures. Peak broadening grain size calculations (Reitfeld analyses) from the diffraction patterns correlate well with those in FESEM images (figure 8).

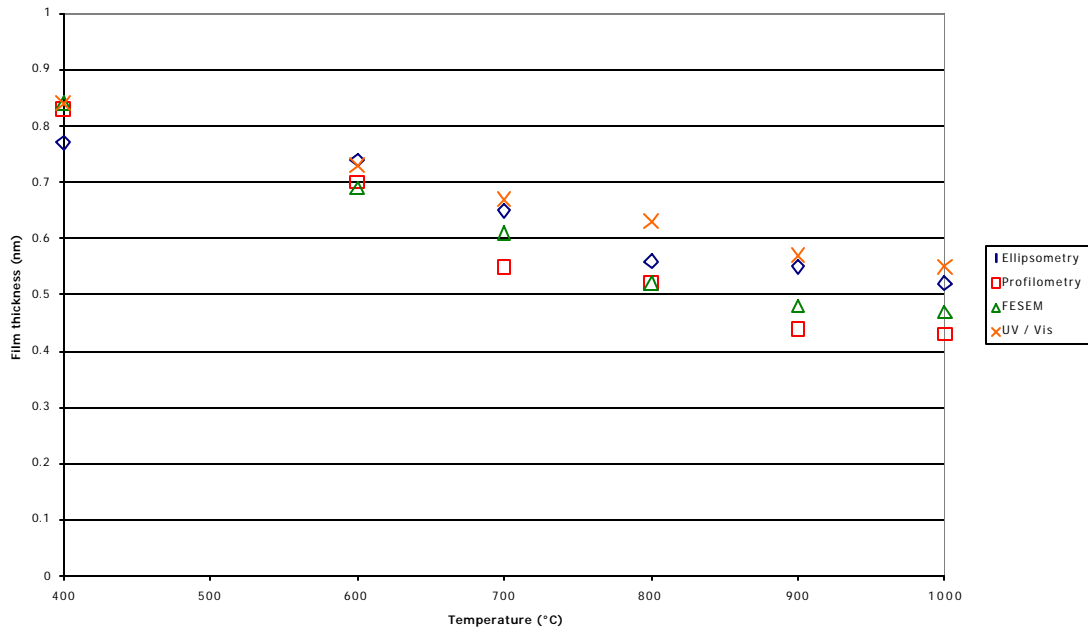


Figure 5. Variation in the film thickness of porous CeO₂ thin films as a function of annealing temperature as measured with different techniques.

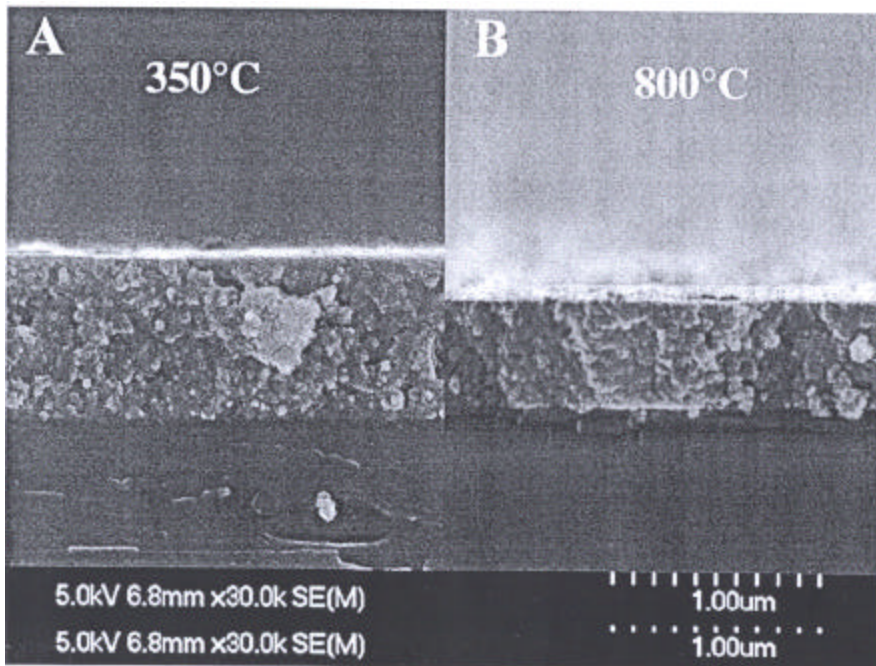


Figure 6. SEM cross-sections of CeO₂ coatings on the sapphire substrate. A, B – after sintering at 400°C and 800°C correspondingly.

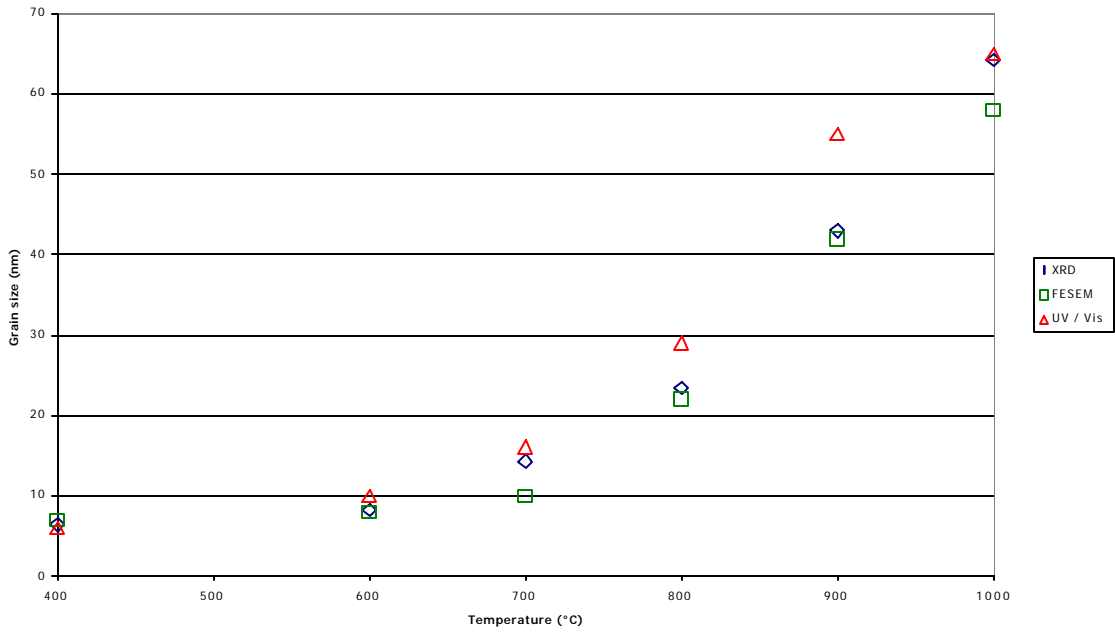


Figure 7. Variation in the grain size of porous CeO₂ thin films as a function of annealing temperature as measured with different techniques.

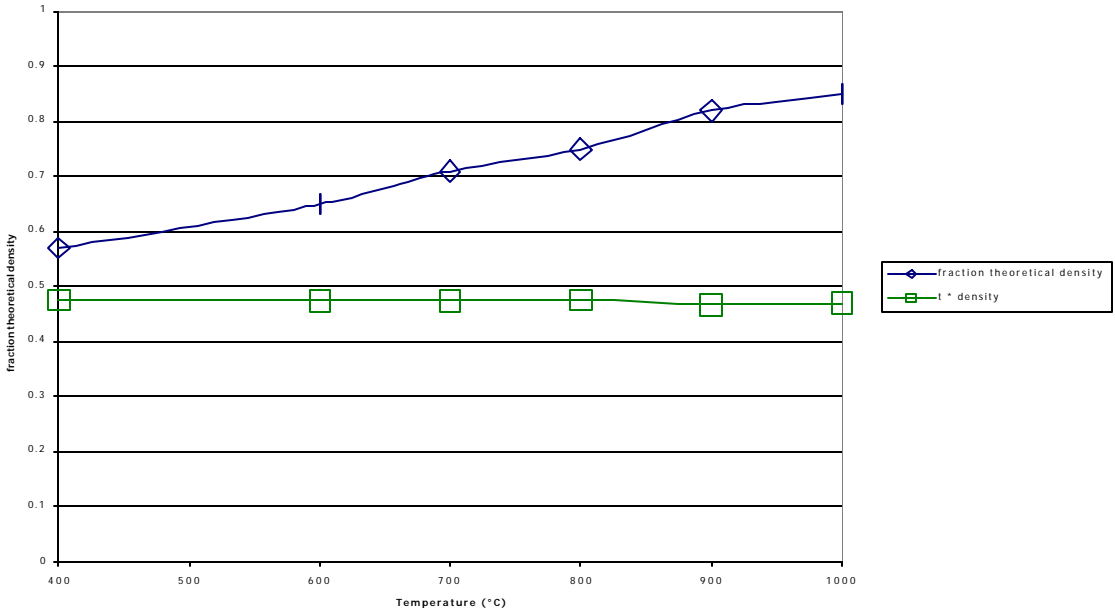


Figure 8. Variation in the density of porous CeO₂ thin films measured with UV/Vis spectrophotometry as a function of annealing temperature.

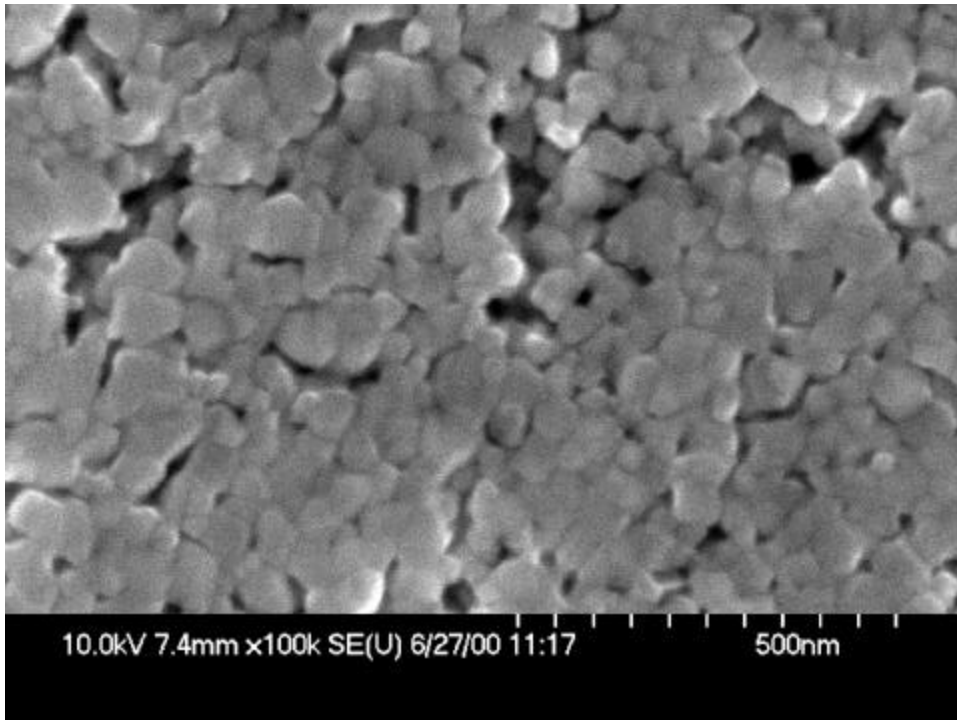


Figure 9. Surface of Ceria film on sapphire which was sintered at 1000°C.

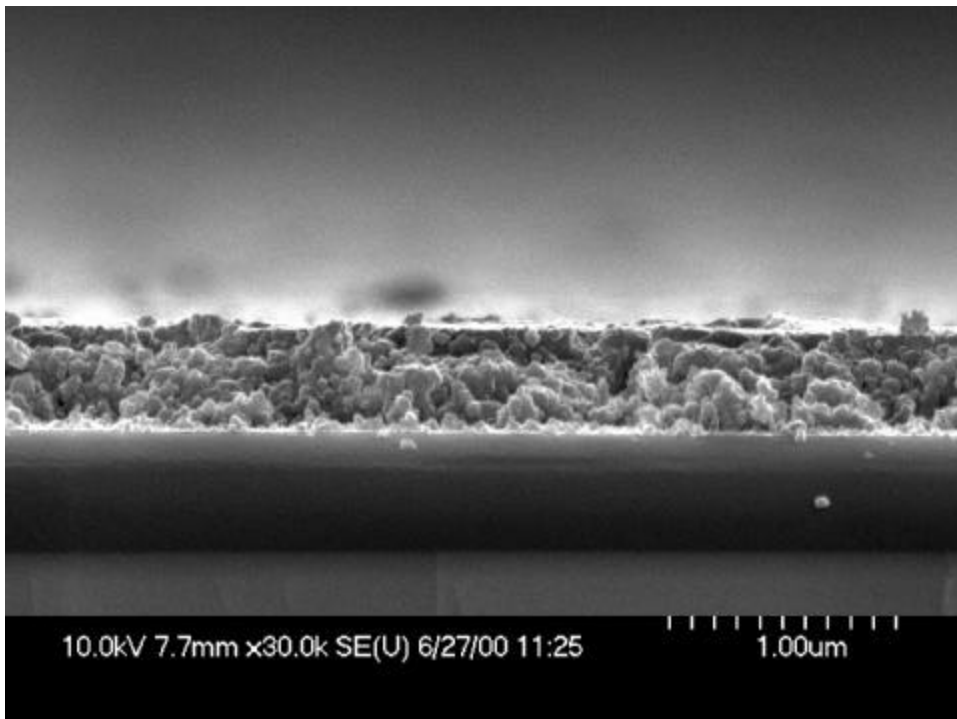


Figure 10. Cross-section of Ceria film on sapphire sintered at 1000°C.

After the initial experiments of depositing ceria onto sapphire had established the deposition process, experiments were started in which the colloidal ceria was deposited onto a porous (La,Sr)MnO₃ (LSM) substrate. Figures 11 & 12 show some of the deposition. Figure 13 shows that a dense zirconia film can be formed on the ceria coating.

The important lessons that have been learned are:

- 1) To be able to form a dense film from polymer precursor solutions on porous substrate, the surface must not have pores that are larger than about 0.2 μ m.
- 2) Colloidal ceria can form a smooth surface on a very porous (>10 μ m diameter pores) surface onto which polymer precursor techniques can be used to produce dense (<1 μ m thick) films.
- 3) The thickness of ceria film must be in the order of the roughness of the underlying substrate before dense films can be formed.

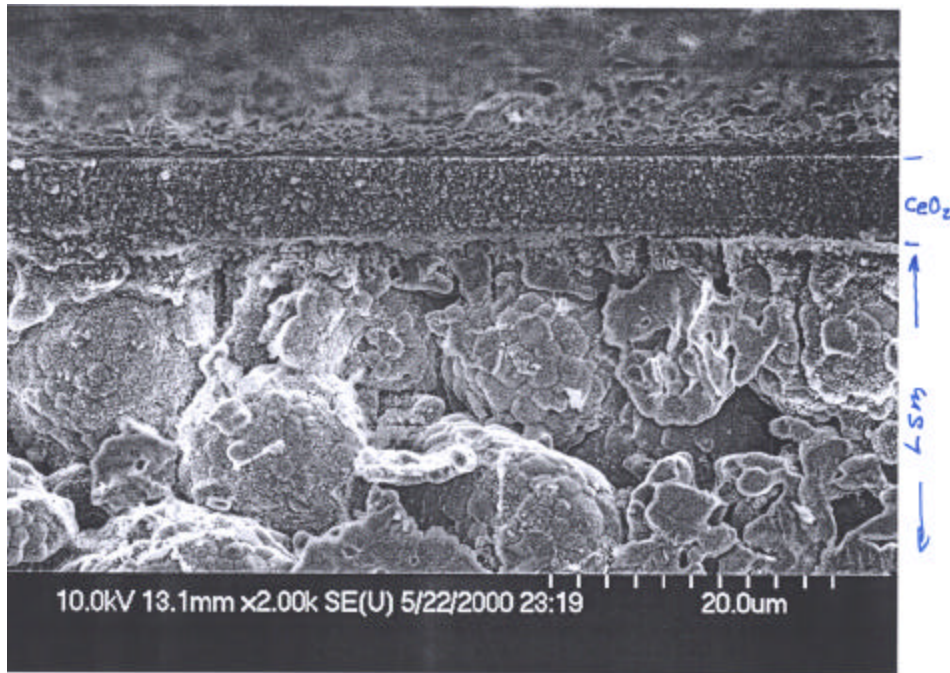


Figure 11. Colloidal CeO₂ porous (60% th. Density) thin film on porous LSM substrate. Composite was sintered at 1000°C.

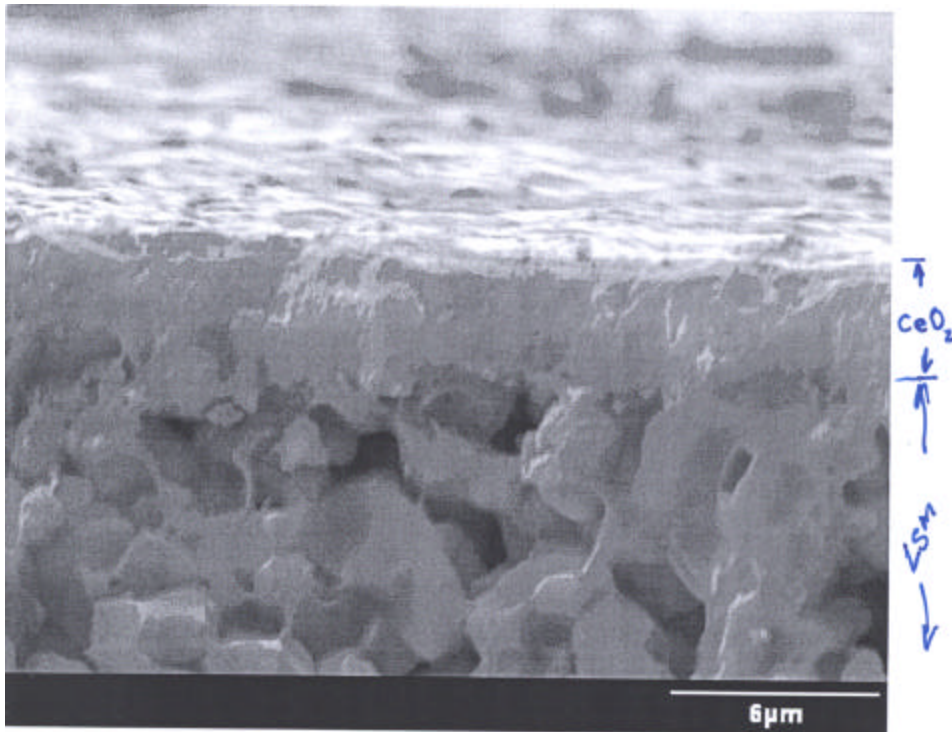


Figure 12. Colloidal ceria planarizing layer. Cross section, high resolution. Sintering temperature of composite = 1000°C .

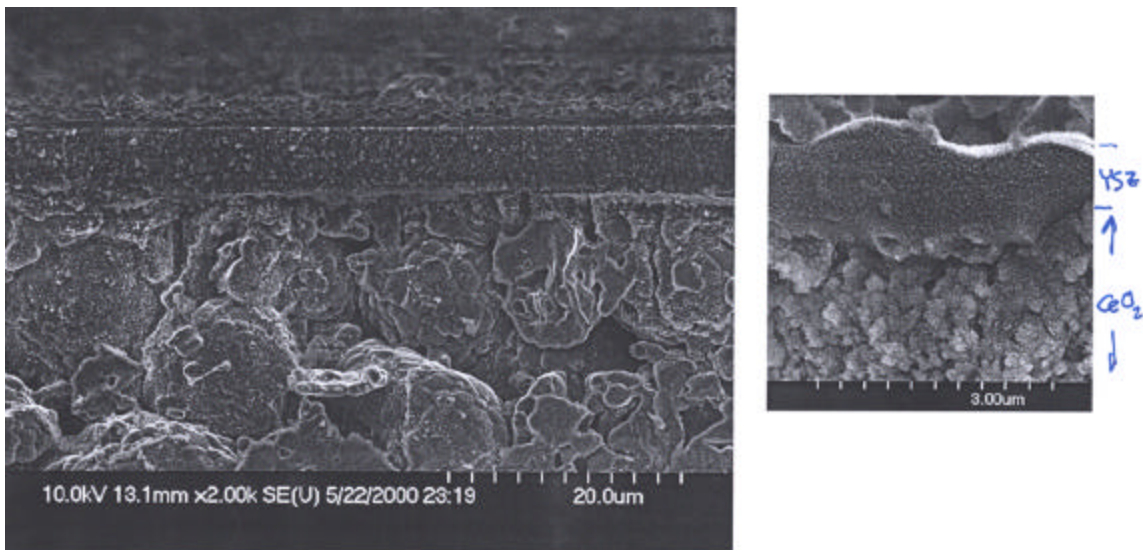


Figure 13. Field-emission SEM micrograph of a YSZ/Colloidal CeO_2 /spray-pyrolyzed LSM composite. $\text{CeO}_2 = 5\mu\text{m}$, YSZ = $0.5\mu\text{m}$. Composite sintered at 800°C .

Neutron Diffraction

Report on preliminary studies of $\text{La}_{0.6}\text{Sr}_{0.4}\text{FeO}_{3-d}$
W. Yelon and Z. Chu

Four samples of the title compound, which had been subject to different heat treatments, were studied using neutron diffraction at the University of Missouri research reactor and the data analyzed using the FULLPROF code for Rietveld analysis. A number of different models were tested based on the parent cubic perovskite structure. Because of the sensitivity of neutron diffraction to the magnetic ordering of the Fe atoms, it was necessary to simultaneously model the magnetic ordering and the nuclear structure. However, the change in magnetic order observed between the air quenched sample and that seen in the reduced samples provided some insight into the physics of these materials.

None of the data sets showed evidence for anything other than single phase materials, except that the 90% CO/10% CO₂ reduced sample is beginning to show peak broadening and asymmetry, suggesting the possibility of incipient decomposition of the sample.

Four models were found to give “reasonable” fits to the data, and each was tested for each sample. The statistical tests, however, show that the preferred model is different for the reduced samples than for the air quenched samples.

There are some notable differences between the neutron diffraction diagrams for the reduced samples and the other (Figures). The diffraction peaks for the reduced samples are significantly sharper than for the other. It was initially assumed that this represented a change to a higher symmetry group with fewer reflections, but no satisfactory fits could be achieved with cubic groups, and the rhombohedral models are the highest symmetry that can satisfactorily fit any (and all) of the data sets. The first diffraction peak (at about 19°) is much stronger in the reduced samples than in the air quenched samples. This peak proves to be purely magnetic and the change reflects a large increase in magnetic moment for the reduced samples vs the air quenched samples.

The Models

Model 1: The first model was found to apply to the air quenched sample. It is a pure rhombohedral (R-3C) space group with unit cell volume around 360 \AA^3 for the tripled hexagonal setting of the cell, i.e. six times the volume of the basic cubic perovskite cell. In this model there is only one oxygen site at the position 0.54 0 0.25. Within this model the magnetic scattering was modeled as antiferromagnetic with moments along the hexagonal c-axis, which reverse between the positions 0 0 0 and 0 0 $\frac{1}{2}$. The magnetic model has the symmetry R-3.

Model 2: refinement of the reduced samples using model 1 left significant residuals in the difference between observed and calculated intensities. Fourier mapping showed that oxygen atoms appeared to (partially) occupy additional positions. Model 2 introduces a second oxygen position (approximate coordinates 0.26, 0.39, 0.07). The occupation of both the normal position

and this additional position were allowed to vary. The magnetic model is the same as employed for model 1.

Model 3: The refinements in model 2 show significant occupation of both the oxygen sites, with a relatively small distance between them. Model 3 examines the possibility that the correct model has only a single oxygen site somewhere between the sites found by model 2. In principle Model 2 should show this directly, by reducing the occupation of the “ideal” octahedral site to zero while filling the second site to the net oxygen occupancy. However, it is not always possible to arrive at such a solution from the starting point for model 2 and thus model 3 is examined separately. The magnetic model is the same as employed for model 1. It is interesting to note that the position for the oxygen refined in this model is significantly different for the reduced samples than for the other one.

Model 4: We decided to test if the symmetry might be lower than rhombohedral by using an orthorhombic space group with dimensions $a^2 \times a^2 \times 2a$, with respect to the fundamental cubic perovskite cell. This cell contains 4 formula units ($240 D^3$) compared to the six formula units in the hexagonal representation of the rhombohedral cell. In this space group there are naturally 2 different oxygen sites, with full occupancies of 4 and 8 respectively. The magnetic structure is modeled in P-1 symmetry, but is essentially the same as in the rhombohedral models.

Results

Table 3 shows some of the results of refinement using these four models. The unit cell volumes (using the R-3C results). The unit cell volumes (using the R-3C results) of the three reduced samples differ by about 0.15%, while they differ from that of air quenched sample by about $5 D^3$. The c/a ratio changes from 2.432 for the air quenched sample to 2.448 for the reduced samples. This change affects the peak positions and the apparent sharpness of the diffraction peaks.

The good ness-of-fit measure X^2 for model 4 is distinctly worse than the best result and this model is discarded. For the air quenched sample model 3 gives a slightly better result than model 1, suggesting that the oxygen atoms are slightly displaced from the “ideal” positions. The difference, however, is slight and might not be significant. All four models show that the oxygen concentration is 3 to within the experimental error of about 0.03. The two-site model fails for these cases.

For the three reduced samples the lowest X^2 is observed for the two site model (model 2). In this case the calculated vacancy concentration increases from 7.2% to 7.8% to 8.8% for the 10% CO, 50% CO and 90% CO samples respectively. It is possible that the octahedra containing oxygen vacancies are distorted from the “ideal” position, while those are fully occupied are close to ideal. It is very likely that correlated motion of adjacent octahedra is actually produced, but further modeling would be necessary to describe this in detail.

The magnetic models for the all five samples are the same, antiferromagnetic Fe coupling the Fe at 0 0 0 with that at 0 0 $\frac{1}{2}$ by a 180° rotation from up to down. However, the Fe moments for the three reduced samples refine between 3.72 and 3.82 μ_B while the moments for the other is much more smaller (1.4 μ_B) for the air quenched sample.

Table 3. La_{0.6}Sr_{0.4}FeO_{3-d}

Sample	1000°C air quenched	1000°C- 10%CO/90% CO ₂	1000°C- 50%CO/50% CO ₂	1000°C- 90%CO/10% CO ₂
<i>Model 1</i>				
chi**2	3.31	16.1	11.6	14.9
% vac	0	6.8	8.1	9.6
Fe moment	1.41	3.81	3.84	3.75
A	5.527	5.54	5.542	5.547
C	13.441	13.56	13.564	13.582
Vol	355.6	360.41	360.84	361.96
<i>Model 2</i>				
chi**2	4.3	8.97	6.6	10.8
% vac	0	7.2	7.8	8.8
Fe moment	1.43	3.82	3.82	3.72
A	5.527	5.54	5.542	5.547
C	13.441	13.56	13.564	13.582
Vol	355.6	360.41	360.84	361.96
<i>Model 3</i>				
chi**2	3.1	9.7	7.06	11.1
% vac	0	7.23	8.41	8.14
Fe moment	1.42	3.86	3.88	3.77
A	5.527	5.54	5.542	5.547
C	13.441	13.56	13.564	13.582
Vol	355.6	360.41	360.84	361.96
<i>Model 4</i>				
chi**2	8.92	14.8	10.2	11.8
% vac	0	8.3	9.1	8.1
Fe moment	1.19	3.74	3.77	3.62
A	5.532	5.541	5.543	5.545
B	5.5	5.536	5.538	5.555
C	7.798	7.833	7.837	7.833
Vol	237.28	240.26	240.54	241.31

Model 1 R-3C symmetry, ideal oxygen octahedral=Ov-refined oxygen concentration

Model 2 R-3C symmetry, partial ideal oxygen Or (x, 0, 0.25, x = 0.533) partial displaced oxygen O5r (0.266, 0.384, 0.074)

Model 3 R-3C symmetry, displaced oxygen only O5s (0.3, 0.37, 0.06)

Model 4 Pbnm symmetry (two oxygen sites) oxygen occupancy refined

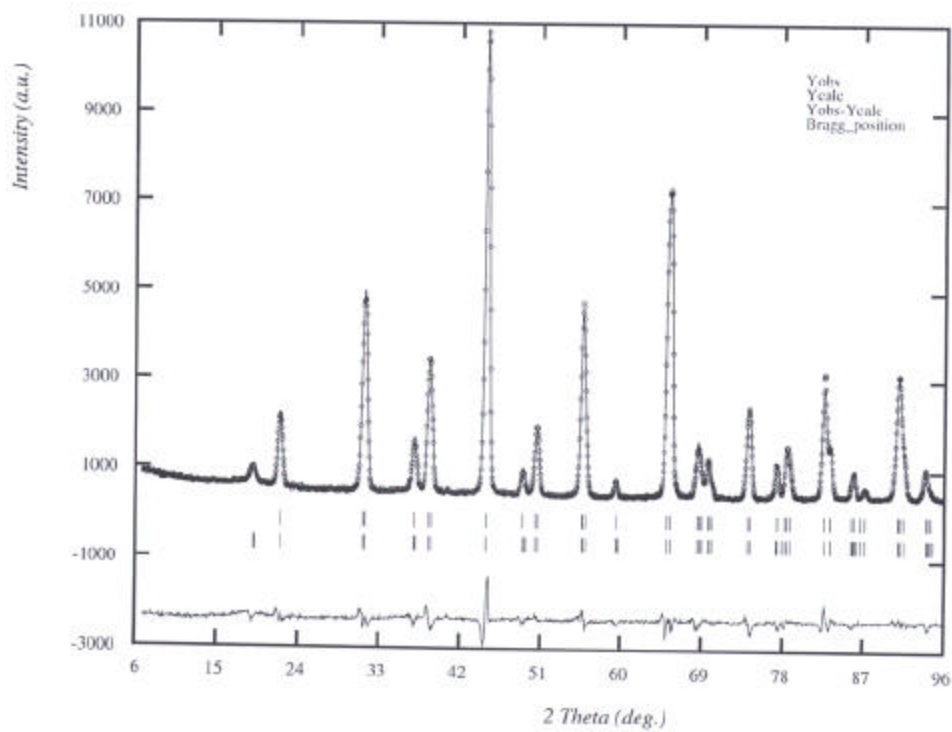


Figure 14. v258 R-3C+R-3mag PSC 1000 Air Quench

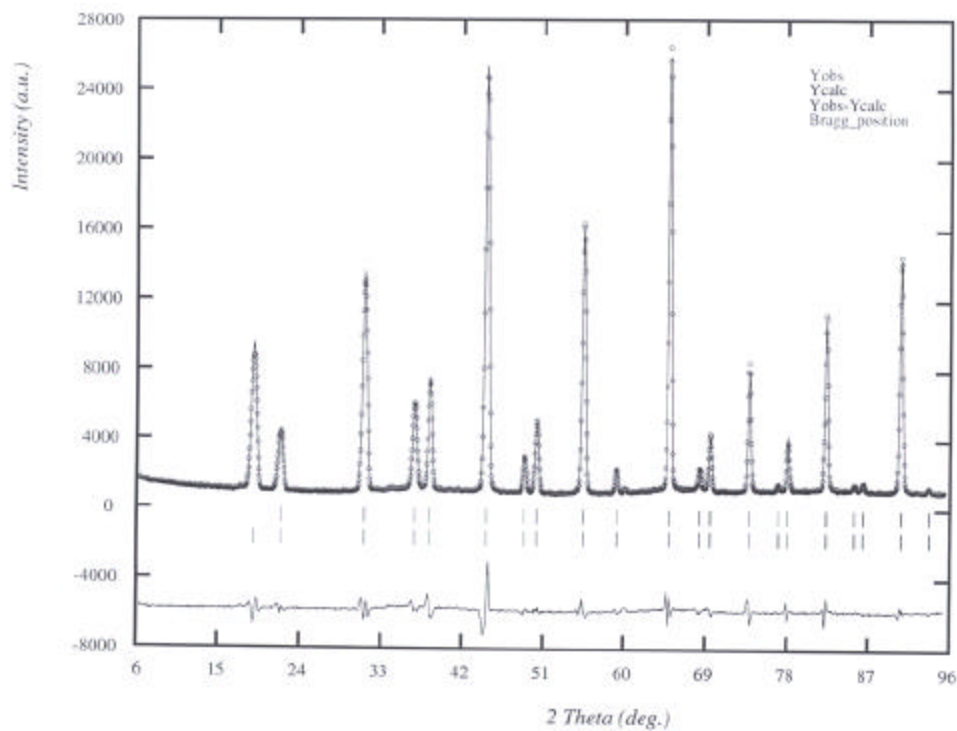


Figure 15. r261 R-3C+R-3mag SPC 1000C Quench 10%CO/90%CO₂

Conclusions

The air quenched sample is close to stoichiometric with less than 1% vacancies on the oxygen lattice. The best refinement has the oxygen atoms at, or very close to their ideal positions in rhombohedral setting of the perovskite cell. The magnetic moment of the Fe is small, around $1.4 \mu_B$.

The oxygen vacancy concentration increases from 7.2% to 8.8% as the reducing treatment changes from 10% CO to 90% CO. The last sample appears to show some sign of decomposition in peak broadening, but can still be refined as a single phase specimen. The estimated standard deviations on the refined vacancy concentration is about 4%. The monotonic change with oxygen partial pressure suggests that the errors may, in fact, be somewhat smaller. Nevertheless, the neutron diffraction should be a good gauge for the following trends.

These experiments are quite straightforward, requiring about 1 g samples and 4-12 hours of data collection depending on the statistical precision desired. Once models are established the refinements proceed rapidly and many models can be tried or data sets analyzed in a brief period.

- For $\text{La}_{0.20}\text{Sr}_{0.80}\text{FeO}_{3-\delta}$, replacing Fe with 35% Cr is not recommended due to SrCrO_4 formation.
 - For $\text{La}_{0.59}\text{Sr}_{0.40}\text{FeO}_{3-\delta}$, replacing Fe with 15% Ti stabilizes the perovskite structure.
 - XRD pattern of $(\text{La}_{0.60}\text{Sr}_{0.40})_{0.99}\text{FeO}_{3-\delta}$ of surface of sintered disk does not show evidence of second phase.
1. Neutron diffraction patterns of $(\text{La}_{0.60}\text{Sr}_{0.40})_{0.99}\text{FeO}_{3-\delta}$ powder show:
- single phase rhombohedral structure (in air at 1000 °C, $\log\text{PO}_2 = -0.7$) and under 10% CO/90% CO_2 ($\log\text{PO}_2 = -12.1$) and 50% CO/50% CO_2 ($\log\text{PO}_2 = -14.1$).
 - decomposition starts under 90% CO/10% CO_2 at 1000 °C ($\log\text{PO}_2 = -16.1$).
- XRD pattern of sintered disk of $\text{La}_{0.60}\text{Sr}_{0.40}\text{Fe}_{0.85}\text{Ga}_{0.15}\text{O}_3$ shows nearly 100% perovskite phase.
 - $\text{La}_{0.20}\text{Sr}_{0.80}\text{GaO}_3$ is multi-phase.
 - Applying a stress on a disk introduces lattice parameter shifts and non-reversible deformation.
 - > 98% theoretical density of $(\text{La}_{0.59}\text{Sr}_{0.40})_{0.99}\text{FeO}_3$ can be reached at a sintering temperature 1200 °C.
 - Colloidal ceria can be used to act as a interface between large pore size substrates ($>10\mu\text{m}$) and dense films.

References

1. M. P. Pechini, "Method of Preparing Lead and Alkaline Earth Titanates and Niobates and Coating Method Using the Same to Form a Capacitor," U. S. Pat. No. 3,330,697, 1967.
2. N. G. Eror and H. U. Anderson, "Polymeric Precursor Synthesis of Ceramic Materials"; pp571-77 in Better Ceramics through Chemistry II, Proceedings of Materials Research Society Symposium, Palo Alto, CA, April 1986. Edited by C. J. Brinker, D. E. Clark, and D. R. Ulrich. Materials Research Society, Pittsburgh, PA, 1986.
3. James Reed, Introduction to the Principles of Ceramic Processing, Chapter 8, pp118-133, John Wiley, New York 1994.
4. J. T. Jones and M. F. Berard, Ceramics: Industrial Processing and Testing, 2nd Edition, pp. 156-177, Iowa State University Press, Ames, Iowa 1993.
5. ASTM C 830-88, "Apparent Porosity, Liquid Absorption, Apparent Specific Gravity and Bulk Density of Refractory Shapes by Vacuum Pressure".
6. ASTM C 20-87, "Apparent Porosity, Water Absorption, Apparent Specific Gravity and Bulk Density of Refractory Brick and Shapes by Boiling Water".

Future

- Further thermal expansion study of $(\text{La}_{0.60}\text{Sr}_{0.40})_{0.99}\text{FeO}_{3.8}$ disk
- Neutron diffraction and modeling study of phase stability, oxygen defect.
- Scheduled study of $\text{La}_{0.60}\text{Sr}_{0.40}\text{Fe}_{0.85}\text{Ga}_{0.15}\text{O}_3$ in task 4.
- Preparing samples to be sent to UIC.
- Expand the preparation of dense films on porous substrate studies.

TASK 5: Assessment of Microstructure of the Membrane Materials to Evaluate the Effects of vacancy-Impurity Association, defect Clusters, and Vacancy Dopant Association on the Membrane Performance and Stability

**Professor Nigel Brown
University of Illinois, Chicago Circle**

Results:

In the last quarter we concentrated on the micro-structural analysis of the decomposition of the (La, Sr)FeO₃ membrane material in-situ (inside the microscope) and ex-situ reduction. For this study we used pellets made from Praxair powders, which were prepared and sintered at 1250° C by the group at University of Missouri, Rolla. After this process the sintered die spent 27 h at 750° C in an oxygen partial pressure of $P_{O_2} = 10^{-2}$ Pa and was finally heated to 800° C in $P_{O_2} = 1 \cdot 10^{-10}$ Pa until a stable equilibrium with its surrounding was reached. The sample was quenched afterwards into an equilibrated atmosphere, i.e. not into air or water. The image from the treated sample at room temperature (figure 1 a) displays some features that were not observed in this sample before. Two dark lines of one unit cell width, separated by one bright line in the center are oriented along the [010] direction. A closer look at those dark lines reveals that a double layer of Fe-O forms its inside. Previous studies have shown that these dark lines result from stacking faults with Fe₃O₄ in the center. This structure can be identified as the Aurivillius phase. Aurivillius phases have the general formula of $(B_2O_2)^{2+} \cdot (A_{m-1}B_mO_{3m+1})^{2-}$. Their structure is composed of m layers of stoichiometric cubic ABO₃ perovskite units, sandwiched between two layers of $(B_2O_2)^{2-}$. In our case m=1 and the layers are composed of $(Fe_2O)^{2+}$. This structure is well established in PbBi₂Nb₂O₉ that was treated at high temperatures and considered as being decomposed.

In-situ reduction of these samples shows that these Aurivillius-phase layers act as nucleation sites for further oxygen vacancy ordering into massive domains, nearly covering the whole grain. The EEL data (figure 1 b) acquired from the bright and dark columns in the ordered oxygen vacancy domains are normalized to the La M-edge intensities. The oxygen K-edge fine structure shows the familiar difference in the pre-peak (532 eV energy loss), which indicates an increased number of oxygen vacancies in the dark columns. From the Fe L₃/L₂ ratio, an Fe-valence that is directly proportional to the concentration of oxygen vacancies can be calculated for the individual columns. The bright, perovskite-like columns exhibit a valence of (2.8±0.1) and the dark, reduced columns a (2.2±0.2) valence. Low magnification X-ray analysis for different grains exhibit significant fluctuations in the atomic ratios of the individual components in the bulk. This analysis infers that individual grains deviate from the ideal stoichiometric composition, due to a segregation of second phases towards the grain boundaries and triple junctions, which causes the Aurivillius phases to build up.

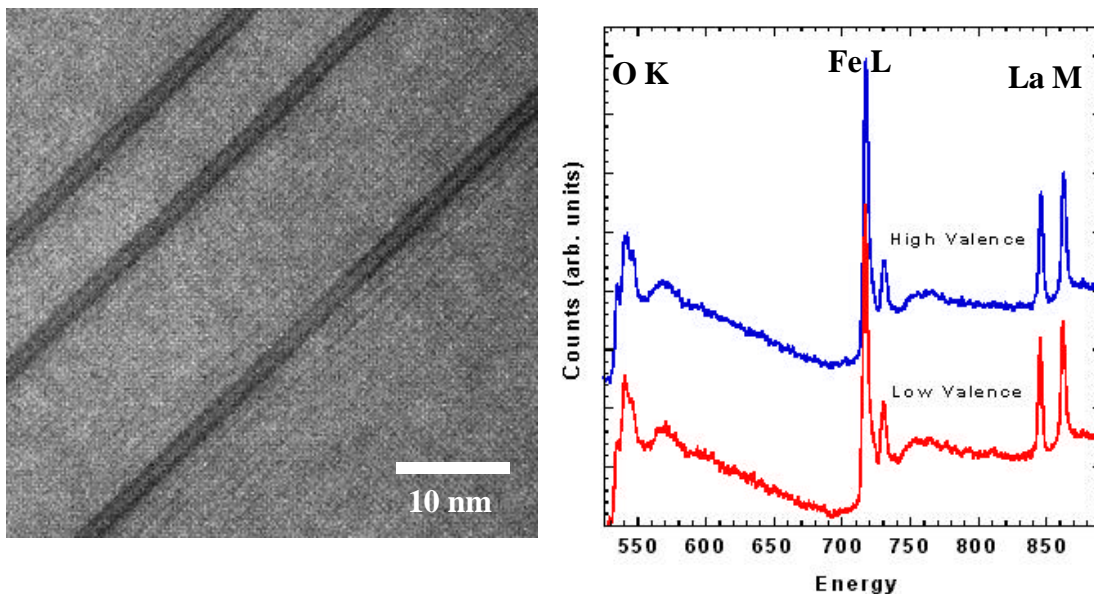


Figure 1: a) Z-contrast image of the decomposed grain, showing the Aurivillius phase. These Aurivillius phases then act as nucleation sites for enormous domains of ordered oxygen vacancies. b) EEL spectra from the bright and dark ordered columns showing the different O K-edge pre-peak as well as the different Fe L-edge ratio.

The correlation of these results to the conductivity measurements, performed by the group of Professor Tuller at MIT, shows that the decomposed material has a highly decreased ionic and electronic conductivity. The reason for the decrease in conductivity can be found from simulations of oxygen mobility (M.S. Islam, *J. Mater. Chem.*, **10**, 2000) which have shown that oxygen flow preferentially occurs parallel to the ordered domains. In the samples before decomposition, the 3-D array of ordered structures therefore allows a high degree of oxygen mobility. After decomposition, each grain acts as a two dimensional conductor, which leads to an overall reduction in the number of pathways for oxygen conduction in the polycrystalline membranes.

In addition the lattice relaxation and changes in the unit cell sizes of the ordered domains and the Aurivillius phases will induce stresses at the grain boundaries of the individual grains. Preliminary studies in collaboration with the group of Professor Bandopadhyay from the University of Alaska have shown that this will lead to an increased fracture probability of the treated and reduced membranes. Further collaboration will explore this effect in greater details and correlate the macroscopic fracture analysis with our microscopy structure analysis.

Task 6: Measurement of Surface Activation/Reaction rates in Ion Transport Membranes using Isotope Tracer and Transient Kinetic Techniques.

Progress during past 3 months at the University of Toronto

Since the review meeting in Boston we have made progress on 3 fronts related to the gradientless isotope infusion experiments. These are: (1) modelling the results to distinguish between redox and simple exchange rates in the isotope infusion experiments, (2) extending the database for infusions in $\text{La}_{0.2}\text{Sr}_{0.8}\text{Fe}_{0.8}\text{Cr}_{0.2}\text{O}_{3-x}$ materials with new samples obtained from BP, and (3) a brief investigation of the effect of surface modification on the rate of oxygen uptake in these materials. There were also some small improvements made to the infusion reactor. The transient experiments on an operating reactor have been delayed again by staffing problems. A new postdoctoral fellow from the Fritz-Haber Institute in Germany will arrive in July to take on this task.

(1) *Redox versus isotope exchange rates during isotope exchange experiments.*

Isotope exchange depth profiling (IEDP) provides a valuable technique for the unambiguous measurement of both bulk mobilities and surface activation rates under unpolarized (chemically equilibrated) conditions. While the oxide ion diffusivities measured by isotopic diffusion in these experiments can be related easily to the bulk conductivities of the material, isotope exchange at the surface can occur by several processes, not all of which are related to the functioning of the material in membrane applications.

For example, we use CO_2 as the exchange gas for low P_{O_2} experiments. Oxygen exchange between the surface and a gas phase species can be achieved by a pure exchange event involving a transient surface intermediate. For example in atmospheres containing CO_2 , isotope exchange between CO_2 and the surface bulk oxide can proceed via surface carbonate intermediates.



Such exchange reactions between CO_2 and oxides are often rapid compared to redox reactions such as the following.



The latter is one of several surface reactions which form part of the oxygen delivery system on the fuel side of the membrane.

By infusing samples using a $C^{18}O_2:C^{16}O$ mixture, the isotope infusion into the sample results from both processes, while the appearance of ^{18}CO in the gas mixture results from process (2) only. We have successfully extended the modeling of such experiments to fit both the mass spectrometric data during the experiment and the resulting infusion profiles. The fits to one such experiment are shown in the previous report.

(3) New infusion experiments/samples:

In Boston (MIT) we presented the latest results obtained for the LaSrCrFeO samples (Praxair). These included both the k and D for diffusion in high oxygen activity (20% O_2) and some for low oxygen activity ($CO/CO_2=1$). It was reported that there were some problems with reproducibility of data on samples from the same batch.

Two samples rods were received in Boston from BP. These samples have since been cut into appropriate sizes and polished down to 0.25 micron in preparation for experiments. The samples were analysed in Houston and were determined to be of high density (97% and 99% of theoretical density). The table below summarizes our work on these samples to date. Two of the BP samples have been infused with 20% oxygen at 750°C and 850°C to compare with previous values on the Houston and Missouri samples.

Experiment	Temperature	Gas	Flow	Status
1	750 °C	20% O_2	10 cc/min	Done
2	850 °C	20% O_2	10 cc/min	Done
3	750 °C	$CO/CO_2 = 1$	10 cc/min	Pending
4	850 °C	$CO/CO_2 = 1$	10 cc/min	Done
5	750 °C	$CO/CO_2 = 1$	20 cc/min	Pending
6	850 °C	$CO/CO_2 = 1$	20 cc/min	Pending
7	750 °C	$CO/CO_2 < 1$	10 cc/min	Pending
8	850 °C	$CO/CO_2 < 1$	10 cc/min	Pending
9	750 °C	$CO/CO_2 < 1$	20 cc/min	Pending
10	850 °C	$CO/CO_2 < 1$	20 cc/min	Pending

These samples did not show any signs of cracking and seem to have maintained their structural integrity during the infusions. In addition one more sample has been infused in a CO/CO₂ mixture with a unity ratio and a low space velocity (10cc/min). This experiment was carried out with a programmed gas flow to prevent carbon deposition during heat up and structural damage during reduction. The sample maintained integrity after quench in LN2. The sample demonstrated surface features which preliminary SEM/EDX analysis indicates to be strontium segregation to the surface (with accompanied surface roughening).

This sample and the previous two are awaiting to be analysed by SIMS to determine their surface reactivity and diffusion coefficients. The parameters derived from the experiment at 850°C in oxygen compared well with those on the previous materials – see table below.

Sample	k_O (cm ² s ⁻¹)	D_O (cm ² s ⁻¹)
BP	2.5×10^{-5}	1.1×10^{-6}
Houston (Praxair powder)	5×10^{-5}	1.5×10^{-6}

Table 1: Comparison of D_O and k_O for two different La_{0.2}Sr_{0.8}Fe_{0.8}Cr_{0.2}O_{3-x} materials

(3) Variability in surface rates on surface modification:

In the last report, and at the MIT review meeting, we showed that irreproducibility is a reality in these experiments. Variabilities of a factor of 2-3 are common. In order to assess the role of surface modification/contamination on the surface exchange rate, we performed a preliminary set of experiments to test the effects of 3 mild surface pretreatments. These were (1) leaching by mild acetic acid (0.01M), (2) contamination by Ni(NO₃)₂ and (3) by HPtCl₄ to produce surface contaminations of approximately 0.5 Pt or Ni per surface La. These were performed on the La_{0.2}Sr_{0.8}Fe_{0.8}Cr_{0.2}O_{3-x} materials from BP. The results are shown in the table below:

Sample	k_O (cm ² s ⁻¹)	D_O (cm ² s ⁻¹)
unmodified	2.5×10^{-5}	1.1×10^{-6}
Pt modified	3.5×10^{-5}	0.3×10^{-6}
Ni modified	1.5×10^{-5}	0.43×10^{-6}
HOAc leached	Failed - sample cracked	-

Table 2: Surface activation rates and diffusion coefficients for La_{0.2}Sr_{0.8}Fe_{0.8}Cr_{0.2}O_{3-x} at 850°C in 20% ¹⁸O₂.

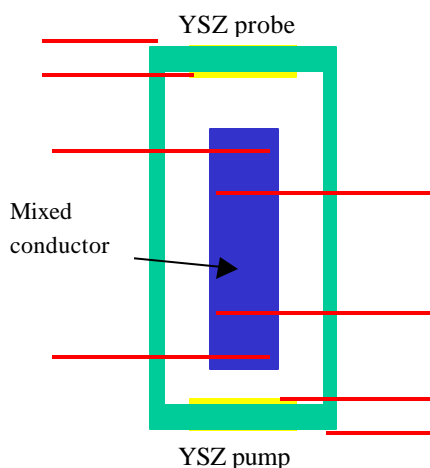
(4) Improvements to the equipment:

Since then we have rebuilt the apparatus and fitted it with a new digital mass flow system to better control the atmosphere during the low PO₂ experiments. This new setup will allow us to program the flow of gasses (CO and CO₂) in order to reduce carbon deposition and prevent samples from cracking under pressure resulting from sudden PO₂ changes. We are currently developing an improvement to our method of preparation of the infused samples for SIMS analysis. There have been problems with cracking and uneven surfaces during the preparation. The new method should result in more detailed SIMS data and hopefully better reproducibility.

Progress during the last 3 months at UH

(1) Conductivity and Stoichiometry of $(\text{La,Sr})\text{Fe}_{0.8}\text{M}'_{0.2}\text{O}_{3-x}$.

Most of our effort in the last three months has involved measurements of the conductivity and stoichiometry of $(\text{La,Sr})\text{Fe}_{0.8}\text{M}'_{0.2}\text{O}_{3-x}$ in sealed cells of the type shown in the Figure. We have



used a four probe ac technique to measure the conductivity at temperatures from 800°C to 1000°C in oxygen partial pressures from 0.2atm to 10⁻¹²atm. Thermodynamic and conductivity data are required for interpretation of the chemical diffusion and exchange measurements to obtain values of D and k that are used to guide the infusion studies. We are also using a lock-in amplifier ac technique in order to measure very small changes in the resistance of the sample. The first set of electrical conductivity results for a second system is

shown below in Figure 4 for five temperatures.

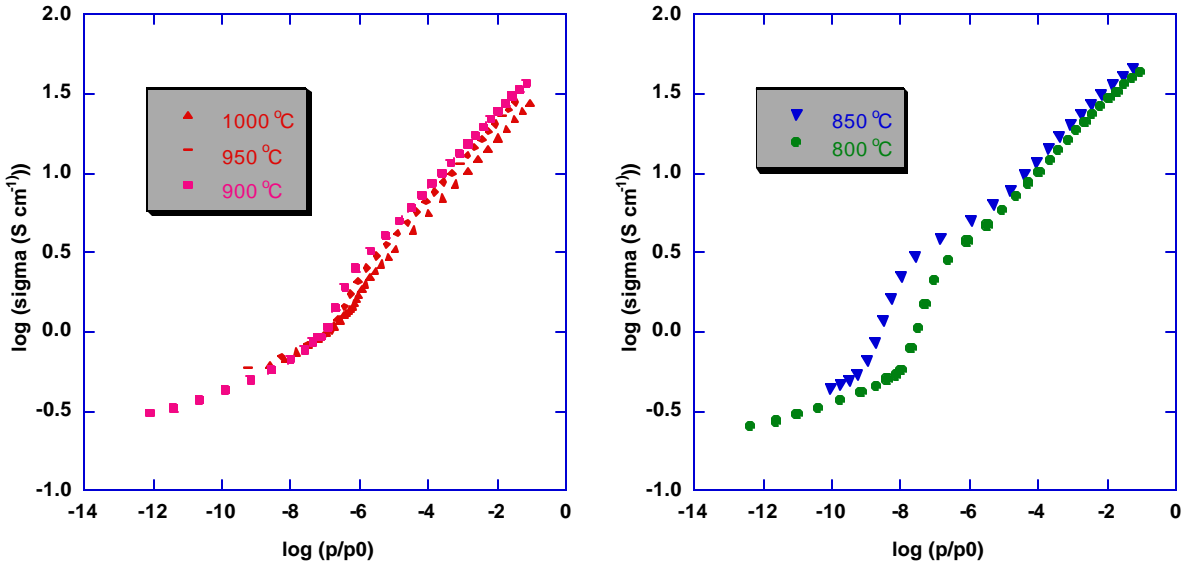


Figure 4. Partial pressure dependence of the electrical conductivity of $\text{La}_{0.5}\text{Sr}_{0.5}\text{Fe}_{0.8}\text{M}'_{0.2}\text{O}_{3-x}$

The data show p type conductivity at high oxygen partial pressures as expected with slopes that are very close to $\frac{1}{4}$ as expected for an ideal p type system with doubly ionized oxygen vacancies. At lower temperatures there is clear evidence for the formation of an intermediate phase presumably as a consequence of vacancy ordering. At intermediate oxygen partial pressures approaching the predominantly ionic transition region, the conductivities are independent of temperature as observed previously for $\text{La}_{0.2}\text{Sr}_{0.8}\text{Fe}_{0.8}\text{M}_{0.2}\text{O}_{3-x}$. A comparison of the two systems is shown in Figure 5 in the higher pressure region. The M system is only linear

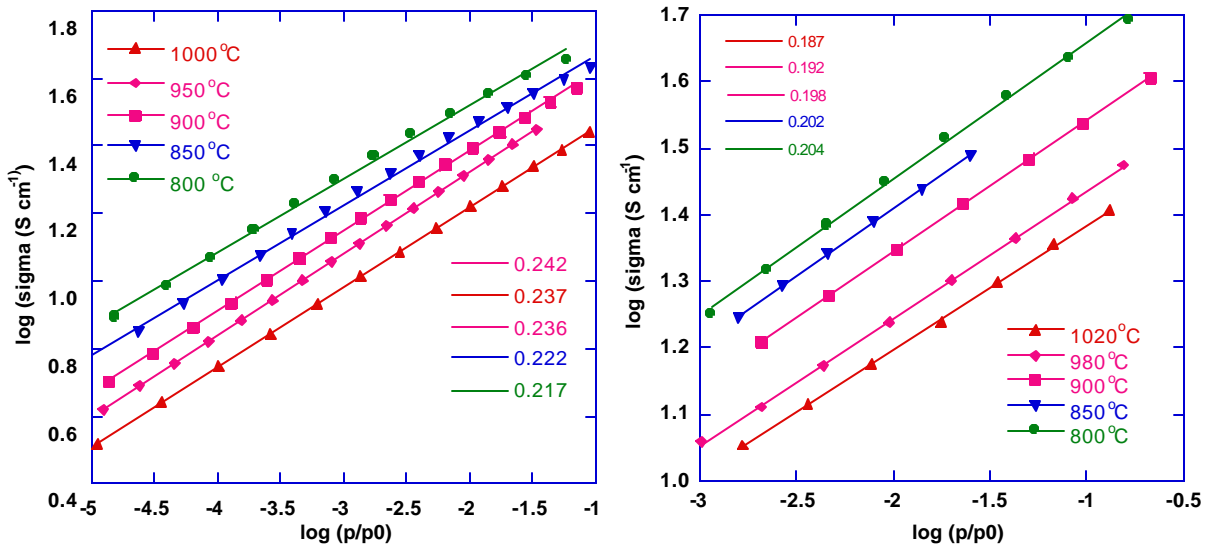


Figure 5 Conductivity data for $\text{La}_{0.5}\text{Sr}_{0.5}\text{Fe}_{0.8}\text{M}'_{0.2}\text{O}_{3-x}$ and $\text{La}_{0.2}\text{Sr}_{0.8}\text{Fe}_{0.8}\text{M}_{0.2}\text{O}_{3-x}$ phases.

down to about $pO_2 = 10^{-3}$ atm whereas the M' system extends to 10^{-5} atm. The slopes of the $\log(pO_2) - \log \sigma$ plots show a greater deviation from $1/4$ for M than for M'. These observations indicate a greater tendency towards vacancy ordering in M than in M'. A comparison of the two sets of data at 800°C is shown in Figure 6.

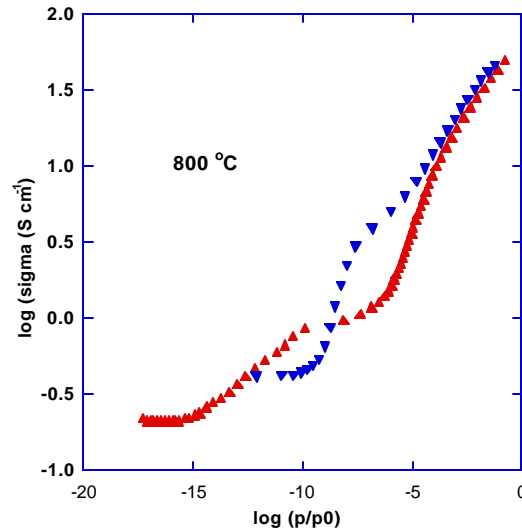


Figure 6 A comparison of M and M' at 800°C

(2) Materials

In order to carry out the isotope transient/membrane experiments at UT, we need to fabricate tubes of the appropriate dimensions. We began with $\text{La}_{0.6}\text{Sr}_{0.4}\text{Fe}_{0.8}\text{Co}_{0.2}\text{O}_{3-x}$ as the material and will also make $\text{La}_{0.2}\text{Sr}_{0.8}\text{Fe}_{0.8}\text{M}_{0.2}\text{O}_{3-x}$ tubes in the future. We have used the sintering protocol that we have developed so far to fabricate discs.

DOE Tasks for next 3 months University of Houston

- (1) We will carry out the analysis of samples from UT by SIMS and reanalyze some of the existing samples after further surface polishing
- (2) We will continue to determine the stoichiometry changes in $\text{La}_{0.2}\text{Sr}_{0.8}\text{Fe}_{0.2}\text{M}_{0.2}\text{O}_{3-x}$ and $\text{La}_{0.5}\text{Sr}_{0.5}\text{Fe}_{0.2}\text{M}'_{0.2}\text{O}_{3-x}$ and verify the reproducibility and reversibility of the data.

DOE Tasks for next 3 months University of Toronto.

- (1) ^{18}O infusion in ferrites in gradientless conditions.

- (a) Further examinations of the oxygen transport in $\text{La}_{0.2}\text{Sr}_{0.8}\text{Fe}_{0.8}\text{M}_{0.2}\text{O}_{3-x}$ under reducing conditions will be performed. We will use $\text{C}^*\text{O}_2/\text{CO}$ mixtures for the infusion, thus establishing a defined oxygen potential, but allowing measurement of the redox process by being able to follow the extent of isotopic equilibration between CO and CO_2 in the mass spectrometer.
- (b) Additional infusions in air will be performed to extend the temperature range on the ferrites above and repeat several of the conditions. We will study new samples recently provided by UH.

(2) Operating membrane experiments

- (a) A new staff member will start the initial shakedown experiments. The initial assembly uses a dense alumina or quartz tube in place of the membrane. This will allow shakedown of the system without risking the perovskite tubes and proved rigorous leak-check to validate the seals. If all goes well, we will then start oxygen permeation measurements (with no reductant on the fuel side) towards the end of the period with the $\text{La}_{0.6}\text{Sr}_{0.4}\text{Fe}_{0.8}\text{Co}_{0.2}\text{O}_{3-x}$ tube currently available.